

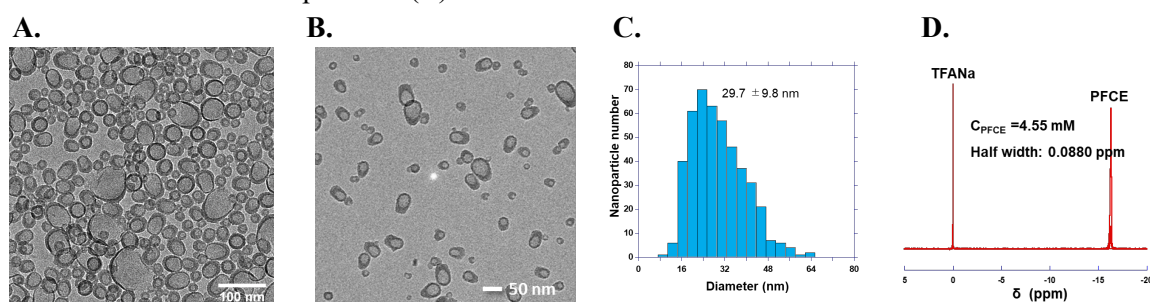
Development of ultrasmall nanoprobe for high sensitivity ^{19}F MRI

(¹Osaka University of Engineering, ²Immunology Frontier Research Center, Osaka University)
Yue Wu¹, Masafumi Minoshima¹, Kazuya Kikuchi^{1,2}

Introduction: Among all the imaging techniques, magnetic resonance imaging (MRI) is of great interest due to its high sensitivity, deep penetration, and noninvasiveness. ^{19}F MRI is an especially powerful tool for bio-imaging benefiting from its negligible background.

Our laboratory has developed FLAME (Fluorine Accumulated silica nanoparticle for ^{19}F MRI Enhancement), a novel ^{19}F MRI nanoprobe enabling efficient ^{19}F MRI *in vivo* [1, 2]. FLAME has a core-shell structure that large amount of liquid perfluorocarbon is coated in silica shell. The structure brings the probe high *in vivo* sensitivity and increased surface modifiability. Despite all the favorable properties, the delivery efficiency of FLAME to cancer tissues is not satisfied. The reason is considered to be size influence that modified FLAME reach up to 100 nm [3]. Therefore, it is considered necessary to prepare nanoprobe with smaller size.

Methods: By suppressing the factor of size increase during nanoparticle synthesis, we managed to synthesis core-shell nanoparticles crude containing ultrasmall nanoparticles (A). Centrifugation was conducted to realize size separation. Dialysis was conducted to purify the obtained ultrasmall nanoparticles (B).



Ultrasmall nanoprobe for ^{19}F MRI

Results and Discussion: TEM image indicated the clear formation of core-shell nanoparticle structure. The ultrasmall nanoparticles has size distribution around 30 nm (C). Peak in ^{19}F NMR confirmed successful encapsulation of perfluorocarbon (PFCE) (D). T_2 measurement indicates that the nanoparticles has similar relaxation properties with PFCE nanoemulsion and FLAME. These results show favorable size distribution and MRI potential of the nanoparticles.

Conclusion: We have successfully manufactured ultrasmall nanoparticles with high MRI sensitivity. The novel ultrasmall nanoprobe is expected to be used for high sensitivity *in vivo* ^{19}F MRI in future experiment. It is expected to obtain a significantly improve targeting efficiency compared with FLAME nanoparticles.

References [1] Matsushita, H. *et al.*, *Angew. Chem. Int. Ed.*, **2014**, 53, 1008-1011.

[2] Nakamura, T. *et al.*, *Angew. Chem. Int. Ed.*, **2015**, 54, 1007-1010.

[3] M. G. Bawendi *et al.*, *Angew. Chem. Int. Ed.*, **2010**, 49, 8649-8652.

All-in-one superparamagnetic radiopaque nanocomplex for *in vivo* MRI, MPI, and CT stem cell tracking

C. Wang^{1,2}, A. Shakeri-Zadeh^{1,2}, S. Kuddannaya^{1,2}, and J.W.M. Bulte^{1,2*}

¹The Russell H. Morgan Department of Radiology and Radiological Science, Division of MR Research, Baltimore, MD, USA;

²Cellular Imaging Section and Vascular Biology Program, Institute for Cell Engineering, Baltimore, MD, USA.

*Corresponding author, email: jwmbulte@mri.jhu.edu

Introduction: Clinical trials using stem cells as a regenerative treatment are on the rise, but in many cases the therapeutic efficacy has been disappointing. The use of *in vivo* imaging techniques to track stem cell trafficking inside the body has considerable potential to enhance therapeutic outcome (1). However, one of the current limitations with *in vivo* cell tracking techniques is that a single imaging modality cannot be responsive to all queries about the fate of transplanted cells, including cell viability, quantity, and overall biodistribution. We aimed to develop a multi-modal cell tracking method using a novel superparamagnetic radiopaque nanocomplex for *in vivo* magnetic resonance imaging (MRI), magnetic particle imaging (MPI), and computed tomography (CT) tracking of mesenchymal stem cells (MSCs), one of the most widely used therapeutic cells in humans.

Methods: **Nanocomplex synthesis and characterization:** Through a simple solvothermal decomposition method, a **BBS** nanocomplex was synthesized composed of bovine serum albumin (**BSA**), radiopaque **Bi₂S₃** nanoparticles and superparamagnetic iron oxide (**SPIO**). BBS nanocomplexes were characterized with dynamic light scattering (DLS), Fourier transform infrared (FTIR) and UV-VIS spectrophotometry, and high-resolution transmission electron microscopy (HR-TEM). Elemental analysis was performed to determine the percentage of iron and bismuth in the BBS nanocomplex. **Cells:** Human bone marrow-derived MSCs (P2) were obtained from Rooster Bio, USA. MSCs were incubated with BBS at a concentration of 25 µg Fe (~125 µg Bi) per ml. Cell labeling was performed with and without poly-L-lysine (1125 ng/ml) as transfection agent in T-75 tissue culture flasks for 24 hours. Labeled cells were collected and prepared for injection in normal male Rag2 mice. Cell viability after incubation with BBS nanocomplex was determined using LDH assay. Prussian blue staining and a Ferrozine-based spectrophotometric assay were used to assess intracellular iron uptake.

Cell transplantation: BBS-labeled MSCs were transplanted in the striatum of Rag2 mice under 1.5% isoflurane anesthesia. Mice were positioned in a stereotaxic device and 100,000 labeled cells in 2 µl of phosphate-buffered saline were injected using a Hamilton syringe (31G, AP=0 mm, ML=2mm, DV= 3 mm, 0.5 µl/min). One hour after transplantation, mice were euthanized and heads were removed and fixed in 4% paraformaldehyde. **Imaging:** A customized holder was 3D-printed for use with all MRI, MPI, and CT machines. One day post fixation, the heads were imaged *ex vivo* with MRI using a 17.6T vertical bore Bruker Biospec scanner and then with MPI using a Magnetic Insight Momentum scanner. *Ex vivo* CT was also performed. MR images were acquired using a FLASH sequence with TR=8.4 ms, TE=2.5 ms, NEX=16, FA=5 deg, resolution=0.1 mm, slice thickness=18 mm, matrix size=150x300x180, and FOV=3x2x1.8 cm. Heads were scanned with MPI using the same FOV as MRI with 55 projections, 3D high-resolution mode, and one scan per projection. Two fiducials containing 25,000 and 50,000 labeled MSCs were placed within the MRI/MPI/CT FOVs and used for cell quantification and data co-registration using 3D slicer software.

Results: BBS nanocomplexes showed a spherical morphology. An even distribution of bismuth, iron and sulfur was found across the BBS spheres, with an average hydrodynamic diameter of 90 nm. The Fe:Bi ratio in BBS nanocomplex was determined as 1:5. FTIR spectra of BSA, SPIO, BSA-Bi₂S₃ nanoparticles, and the overall BBS nanocomplexes confirmed the covalent bonds between BSA, Bi₂S₃ nanoparticles and SPIOs. Prussian blue staining showed peri-nuclear accumulation of nanocomplex in labeled MSCs, with an iron content of 17 pg Fe per cell. No significant cytotoxicity was found for BBS nanocomplex. Using *ex vivo* imaging data, the location of transplanted cells could be easily addressed by MRI and CT, while the number of cells was quantified using MPI.

Discussion: We demonstrated the possibility of multi-modal imaging of transplanted cells with trimodal imaging using a single composite nanocomplex. In addition to visualization of cells with an anatomical context provided by CT and MRI, another benefit of using BBS nanocomplexes as a cell labeling agent is the ability to quantify cell content with MPI (2, 3). Since BBS is a cold tracer (without radioactivity), it may also allow easy-to-interpret whole-body distribution studies when BBS-labeled MSCs are injected systematically. Further studies are being performed in our lab to assess the effects of BBS on stem cell differentiation into adipocytes, chondrocytes and osteocytes.

Conclusion: We successfully developed a novel nanocomplex for labeling and tracking stem cells using multi-modal imaging.

References: **1)** A.K. Srivastava, et al. Seeing stem cells at work in vivo. *Stem Cell Reviews and Reports*. **2014**; 10:127. **2)** J.W.M. Bulte, Superparamagnetic iron oxides as MPI tracers: A primer and review of early applications. *Advanced Drug Delivery Reviews*. **2019**; 138:293. **3)** J.W.M. Bulte, et al., Quantitative “hot-spot” imaging of transplanted stem cells using superparamagnetic tracers and magnetic particle imaging. *Tomography*. **2015**;1(2):91.

Exploring the use of Iron(III) Metal-Organic Polyhedra as Magnetic Resonance Imaging Contrast Agents for Murine Tumor Models

Authors: Gregory E. Sokolow,¹ Matthew R. Crawley,¹ Joseph A. Sperryak,² Timothy R. Cook,¹ and Janet R. Morrow¹

¹ Department of Chemistry, University at Buffalo the State University of New York, Buffalo, NY 14260.

² Department of Cell Stress Biology, Roswell Park Cancer Institute, Buffalo, NY 14263.

Introduction: Fe(III) complexes have been examined as magnetic resonance imaging (MRI) contrast agents for T₁-weighted imaging.¹⁻³ We have repurposed metal-organic polyhedra (MOPs) previously explored for catalysis⁴⁻⁵ to incorporate Fe(III) metal centers tethered with rigid-organic linkers resulting in highly anionic complexes that hold promise as contrasts for MRI. Altering the morphologies of these MOPs drastically affects the observed bio-distribution while maintaining proton relaxation properties associated with shared Fe(III)-catecholate coordination environments.

Methods: Synthesis: Fe₄A₆ and Fe₂C₂(μ-OCH₃)₂ were synthesized with careful stoichiometric control in methanolic solutions.⁶ Characterization: A combination of ¹H NMR, FT-ICR-MS, ICP-MS, EPR, and single crystal XRD were used to characterize these MOPs and subsequent diamagnetic Ga(III) analogs. Complexes were assessed for iron dissociation by monitoring ligand to metal charge transfer(LMCT) bands characteristic for Fe(III)-catecholate complexes under anionic, cationic, and pH stress as well as with competitive assays with EDTA. Protein interactions: Human serum albumin(HSA) binding was assessed using combinations of free iron determination by a ICP-MS/filtration method and by fitting measured relaxation rate data from MOP/HSA titrations. In vitro relaxivity: T₁ relaxivities were assessed at 4.7 T, 37 °C on an MRI scanner by inversion-recovery balanced steady-state free precession (bSSFP) acquisitions as well as at 1.4 T, 34 °C using inversion-recovery experiments. Contrasts were examined with and without HSA (35 mg/mL) in 1x PBS buffered solutions at pH 7.4. In vivo MRI: MR imaging was performed at a magnetic field strength of 4.7 T in accordance with approved Roswell Park IACUC protocols. Female mice were inoculated subcutaneously with VEGF-modified ID8 ovarian cancer cell lines and tumors were grown to approximately 25 mm³ (25.3 ± 7.8 mm³). Three-dimensional, spoiled gradient echo (SPGR) scans of the upper thorax to hindquarters were collected and assessed pre-injection (acquisition parameters: TE/TR/FA = 3/15/40°, FOV = 48x32x32 mm, acquisition matrix = 192x96x96, scan duration = 2.75 minutes). Contrast agents were administered intravenously via the tail vein. Scans were acquired continuously up to 75' post-injection with supplemental scans at 4 h and 24 h post-injection.⁶

Results: Fe₄A₆ was determined to be robust to iron dissociation under the examined conditions while Fe₂C₂(μ-OCH₃)₂ in the presence of excess EDTA resulted in the disappearance of the characteristic LMCT band. Both complexes showed enhancement in T₁ relaxivities in the presence of HSA indicative of a binding interaction. Fe₄A₆ displayed nearly a three-fold increase in the observed T₁ relaxivity at 4.7 T, 37 °C in the presence of HSA (8.7 ± 0.1 to 21 ± 0.1 mM⁻¹s⁻¹).⁶ It was possible to elucidate up to 5:1 binding for the MOP to a single globular protein by observing the T₁ relaxation rate of solutions containing increasing concentrations of Fe₄A₆ with 10 μM HSA. The average association constant for five binding events of Fe₄A₆ with HSA was determined to be greater than 10⁴ M⁻¹.⁶ Accumulation of Fe₄A₆ was observed in subcutaneous tumor models with contrast enhancements observed 24 h post-injection. Fe₂C₂(μ-OCH₃)₂ did not show significant image enhancements to subcutaneous tumors with significantly higher renal clearance observed when compared to Fe₄A₆.

Discussion: Protein binding plays a crucial role in controlling the in vivo properties of these MOPs. Increased T₁ relaxivities are likely a result of slowed molecular tumbling for these anionic rigid MOPs upon the formation of larger protein/contrast adducts. The strong binding interaction of Fe₄A₆ to HSA also influences the contrasts residence time in the vascular system and results in a hepatobiliary clearance pathway.⁶ It is also likely that the overall size of the globular protein adduct contributes to the prolonged enhancement in subcutaneous tumor models taking advantage of enhanced permeability and retention effects. Fe₂C₂(μ-OCH₃)₂ was observed to clear the vascular system with a combination of renal/hepatobiliary mechanisms. It is possible that a significant reduction of anionic charge weakens the binding interactions with blood pool proteins enabling these smaller MOPs to clear through a renal mechanism while mitigating enhancements in subcutaneous tumor models.

Conclusion: Utilizing self-assembly and Fe(III)-catecholate coordination environments it is possible to generate MR contrast agents with varied in vivo properties while maintaining suitable relaxivities for imaging applications. We have been able to successfully image ID8 subcutaneous tumor models with prolonged image enhancements out to 24 h post-injection. These model complexes lay the foundation to further explore the structure-functional relationship of Fe(III)-catecholate assemblies for MR imaging applications.

References: 1. Snyder, E. M.; Asik, D.; Abozeid, S. M.; Burgio, A.; Bateman, G.; Turowski, S. G.; Sperryak, J. A.; Morrow, J. R., A Class of Fe(III) Macrocyclic Complexes with Alcohol Donor Groups as Effective T₁ MRI Contrast Agents. *Angew. Chemie. Int. Ed.* 2020. 2. Wang, H.; Jordan, V. C.; Ramsay, I. A.; Sojoodi, M.; Fuchs, B. C.; Tanabe, K. K.; Caravan, P.; Gale, E. M., Molecular Magnetic Resonance Imaging Using a Redox-Active Iron Complex. *J. Am. Chem. Soc.* 2019. 3. Bales, B. C.; Grimmond, B.; Johnson, B. F.; Luttrell, M. T.; Meyer, D. E.; Polyanskaya, T.; Rishel, M. J.; Roberts, J., Fe-HBED Analogs: A Promising Class of Iron-Chelate Contrast Agents for Magnetic Resonance Imaging. *Contrast Media Mol. Imaging* 2019. 4. Caulder, D. L.; Brueckner, C.; Powers, R. E.; Koenig, S.; Parac, T. N.; Leary, J. A.; Raymond, K. N., Design, Formation and Properties of Tetrahedral M₄L₄ and M₄L₆ Supramolecular Clusters. *J. Am. Chem. Soc.* 2001. 5. Hong, C. M.; Bergman, R. G.; Raymond, K. N.; Toste, F. D., Self-Assembled Tetrahedral Hosts as Supramolecular Catalysts. *Acc. Chem. Res.* 2018, 6. Sokolow, G. E.; Crawley, M. R.; Mophet, D. R.; Asik, D.; Sperryak, J. A.; McGray, A. J. R.; Cook, T. R.; Morrow, J. R., Metal-Organic Polyhedron with Four Fe(III) Centers Producing Enhanced T₁ Magnetic Resonance Imaging Contrast in Tumors. *Inorg. Chem.* 2022.

MPI/MRI of cerebral homing of SPIO-labeled stem cells after intra-arterial injection

A. Shakeri-Zadeh^{1,2}, S. Kuddannaya^{1,2}, A. Bibic^{1,3}, P Walczak⁴, and J.W.M. Bulte^{1,2,3*}

¹The Russell H. Morgan Department of Radiology and Radiological Science, Division of MR Research, Baltimore, MD, USA; ²Cellular Imaging Section and Vascular Biology Program, Institute for Cell Engineering, Baltimore, MD, USA; ³F.M. Kirby Research Center for Functional Brain Imaging, Hugo W. Moser Institute, Kennedy Krieger Inc., Baltimore, MD, USA; ⁴Department of Diagnostic Radiology and Nuclear Medicine, University of Maryland School of Medicine, Baltimore, MD, USA.

*Corresponding author, email: jwmbulte@mri.jhu.edu

Introduction: In several pre-clinical and clinical studies, it has been demonstrated that cell therapy is a promising method to treat stroke. Intra-arterial (IA) injection using the carotid artery is an attractive administration route as it prevents initial uptake by systemic organs delivering large numbers of cells directly to brain (1). Information on the effectiveness of the procedure and amount of delivered cells is highly desirable for further optimization. In this study, we used magnetic particle imaging (MPI) combined with magnetic resonance imaging (MRI) to track human mesenchymal stem cells (hMSCs) labeled with superparamagnetic (SPIO) nanoparticles *in vivo* (2, 3).

Methods: Commercially available bone marrow-derived hMSCs (Rooster Bio, USA) were magnetically labeled with and without poly-L-lysine (1125 ng/ml) as transfection agent and the commercial SPIO formulation Resovist® (25 µg Fe/ml) in T-75 tissue culture flasks for 24 hours. Labeled cells were collected and prepared for IA injection into normal male Rag2 mice (n=3). Prussian blue staining and a Ferrozine-based spectrophotometric assay were used to assess intracellular iron uptake. Animal surgery and IA injection was performed as shown in **Figure 1A** and recently described elsewhere (4). Labeled cells were delivered into brain using 4 separate injections (30,000 cells each) with a time interval of 6 min between each injection. Whole body standard 2D MPI was performed before and after each injection. A final 2D MPI scan was obtained 30 min after the last injection. Animals were then sacrificed and the heads were imaged *ex vivo* with MRI using a 17.4T vertical bore Bruker Biospec scanner and then with MPI using a Magnetic Insight Momentum scanner. MR images were acquired using a FLASH sequence with TR=8.4 ms, TE=2.5 ms, NEX=16, FA=5 deg, resolution=0.1 mm, slice thickness= 18 mm, matrix size=150x300x180, and FOV=3x2x1.8 cm. Heads were scanned with MPI using the same FOV as MRI with 55 projections, 3D high resolution mode, and one scan per projection. A customized holder was 3D-printed for use with both MRI and MPI. Two fiducials containing 10,000 and 20,000 labeled hMSCs were placed within the MPI and MRI FOVs and used to register the MPI dataset with MRI using 3D slicer software.

Results: Microscopic examination of a droplet of live cell suspension showed successful labeling of hMSC (**Figure 1B**, right bottom panel), which was later confirmed with Prussian blue staining. Figure 1B, left side, shows peri-nuclear accumulation of SPIOs in labeled hMSCs. An amount of 25 pg Fe per cell was measured by the Ferrozine assay. **Figure 1C** shows representative individual and overlay images of the *ex vivo* MRI and MPI datasets, where a unilateral distribution of labeled hMSCs at the side of IA injection can be seen. **Figure 1D** shows MP images of a mouse before and after IA injection, where hot spots in brain and lung as well as signal intensity alterations over time are clearly recognizable.

Discussion: When performing clinical stem cell transplantation studies, e.g., IA cell delivery to stroke patients, a main query is the number of cells that have arrived at the targeted tissue site and their spatial biodistribution. MPI/MRI hybrid imaging of magnetically labeled cells is a proper technique to address this issue. Aside from having quantitative and structural information together, the chief advantage of MPI/MRI hybrid imaging is the utilization of cold tracers (without radioactivity), allowing easy-to-interpret whole-body distribution studies. As shown in **Figure 1C**, our MPI/MRI data clearly show cerebral homing of labeled hMSCs after IA injection so that any region of interest can be quantified.

Conclusion: This successful example MPI/MRI application of *in vivo* tracking of hMSCs may encourage further use of this technique to probe the fate of therapeutic cells after transplantation.

References: 1) B. Rodríguez-Frutos, et al., Stem cell therapy and administration routes after stroke, *Translational stroke research*. **2016**; 7(5):378. 2) J.W.M. Bulte, Superparamagnetic iron oxides as MPI tracers: A primer and review of early applications. *Advanced Drug Delivery Reviews*. **2019**; 138:293. 3) J.W.M. Bulte, et al., Quantitative “hot-spot” imaging of transplanted stem cells using superparamagnetic tracers and magnetic particle imaging. *Tomography*. **2015**;1(2):91. 4) C. Chu, et al., Hyperosmolar blood-brain barrier opening using intra-arterial injection of hyperosmotic mannitol in mice under real-time MRI guidance. *Nature Protocols*. **2022**; 17, 76.

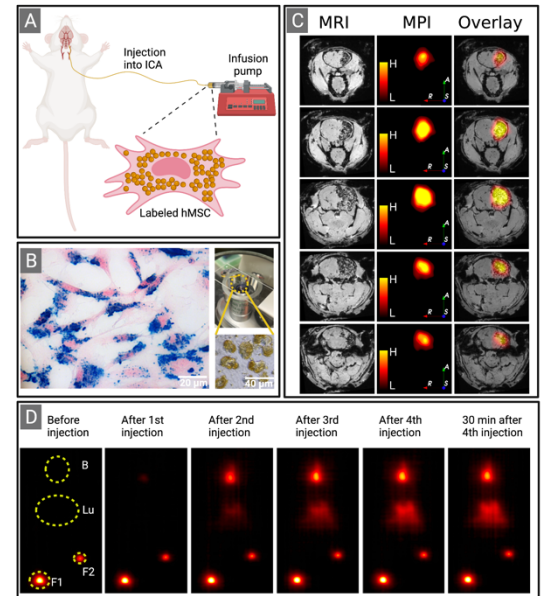


Figure 1. (A) Schematic outline of IA injection of Resovist-labeled hMSCs into the internal carotid artery (ICA). (B) Prussian blue staining of labeled hMSCs along with a microscopic image of live labeled cells before injection. (C) Five MPI/MRI slices from forebrain to midbrain (top to bottom) of a mouse injected with 120,000 labeled hMSCs. (D) Serial MPI images of a mouse before and after IA injection. In this panel, B, Lu, F1, and F2 stand for brain, lung, first fiducial (20,000 labeled hMSCs) and second fiducial (10,000 labeled hMSCs), respectively.

Monitoring Scaffolded Glial-Restricted Progenitor Cell Survival and Hydrogel Degradation in the CNS of ALS mice

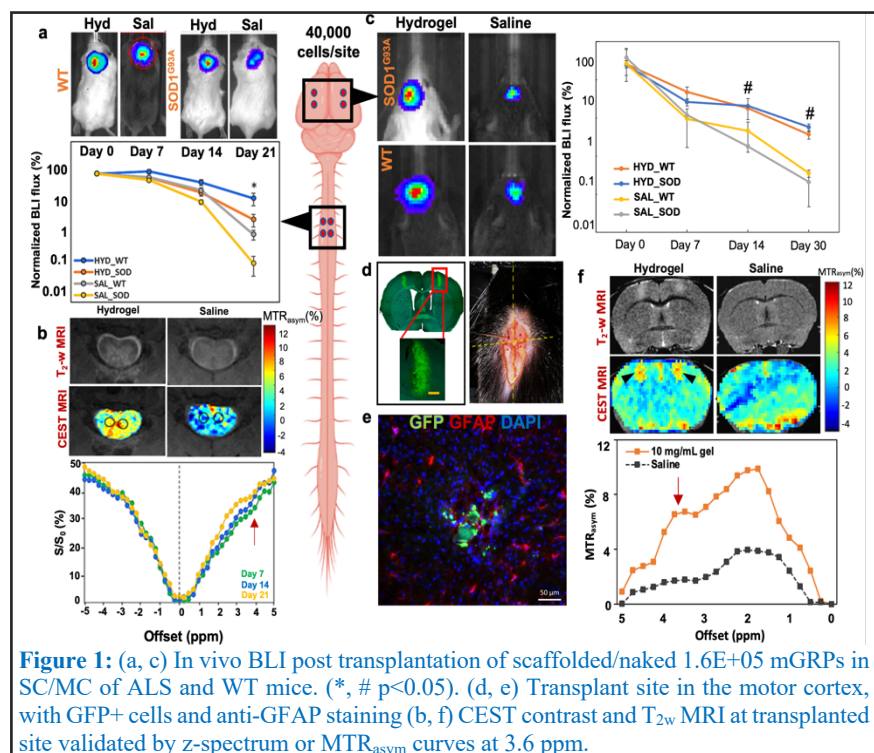
Shreyas Kuddannaya¹, Sarah K. Gross², Nicholas J. Maragakis², Jeff W.M. Bulte¹

¹Cellular Imaging Section, Institute for Cell Engineering and Russell H. Morgan Department of Radiology and Radiological Science, Johns Hopkins University SOM, Baltimore, MD, USA, ²Department of Neurology, Johns Hopkins University SOM, Baltimore, MD

Introduction: Cell therapies of the central nervous system (CNS) are hampered by high initial cell death and a host graft rejection leading to a cell loss of >90% of transplanted cells within 1 week of transplantation. Diseased microenvironments such as in amyotrophic lateral sclerosis (ALS) can further compromise cell therapy due to high inflammation and astrogliosis¹. We hypothesize that scaffolding cells in composite hyaluronic acid (HA)-based gels can significantly improve transplanted cell survival as evidenced by serial bioluminescence imaging (BLI). Concurrently we aim to assess hydrogel degradation quantitatively via chemical exchange saturation transfer (CEST) MRI due to abundant high amide protons of gelatin component of gels², without necessitating any exogenous labels.

Methods: Cells: Allogeneic A2B5⁺ murine glial-restricted progenitors (mGRPs) carrying proteolipid protein-green fluorescent protein (PLP-GFP) gene were derived from fetal forebrain tissue of (E13) transgenic mice and transduced with a lentiviral vector carrying firefly luciferase (pLenti4-CMV-Luc) gene. Gel formulation: Composite hydrogels were formulated by mixing thiolated HA (HA-S), thiolated gelatin (Gel-S) and poly (ethylene glycol) diacrylate (PEGDA) crosslinker in ratio 2:2:1 at various concentrations and their rheological properties were tested. Transplantation: Based on optimal stiffness, injectability and high cell viability, 10 mg/ml gel formulation was chosen and a total of 1.6×10^5 cells (4×10^4 cells/site) were transplanted bilaterally at 4 sites either in the ventral horns of C3-C4 cervical spinal cord (SC) or in the motor cortex (MC) of the SOD1^{G93A} mouse model of ALS via stereotaxic microsurgery (Figure 1d). MRI was performed on 11.7T horizontal bore Bruker Avance scanner equipped with 15 mm birdcage transmit/receive coil using rapid acquisition and relaxation enhancement (RARE) pulse sequence. Imaging parameters: slice thickness=1.5 mm, Averages= 2, Echo time=19 ms, Relaxation time= 1500 ms, matrix size=128x128, Field of view (FOV)=17x17 mm² and RARE factor=16. For CEST imaging, a saturation power of B1= 3.6 μ T was used with -5.5 to 5.5 ppm offset range.

Results: The survival of scaffolded vs. naked mGRPs transplanted in SC/MC of the ALS and WT mice was serially monitored by BLI at least until 4 weeks post injection. In the CNS, the BLI signal gradually decreased during subsequent weeks in both hydrogel-scaffolded and naked (saline) groups but decreased significantly in the saline group post-day 7 ($p < 0.05$) (Figure 1a, c). At endpoint (>4 weeks) scaffolded mGRPs showed significantly higher BLI signal intensity in both MC and SC accounting for a ~4.5-fold increase in transplanted cell survival compared to naked cells. T₂-w MRI revealed a hyperintense signal at the injection site owing to higher water content of hydrogel matrix, which diminished in size over time. In contrast, the CEST signal was found to be specific for the exchangeable protons within the hydrogel, which enables monitoring the hydrogel degradation fates in real time. CEST signals were assessed in terms of *in vivo* MTR_{asym} spectra which revealed two peaks at 0.5–2.0 and 3.6 ppm (Figure 1b, f). Immunohistology with anti-GFAP antibody staining revealed that the activated astrocytes were confined at the graft periphery (Figure 1e).



Discussion: Cell transplantation in the CNS of the SOD1^{G93A} mice indicated higher scaffolded cell survival and proper bio-clearance of the gel. Only at the hydrogel injected site did the MTR_{asym} values at 3.6 ppm show a progressive decrease. There was no CEST contrast at the injection site for the saline control group (naked mGRPs). Importantly, we noted that the presence of mGRPs in the hydrogel scaffold (or saline control) did not significantly alter the CEST spectra showing negligible contrast at 3.6 ppm supporting the specificity of CEST MRI for amide protons in gelatin.

Conclusion: We demonstrated that hydrogel morphology and biodegradation can be concurrently monitored in a label-free manner *in vivo* via T₂-w MRI and CEST MRI respectively, with the hydrogel acting as a barrier for infiltrating host immune cells. Serial *in vivo* BLI revealed a 4.5-fold enhancement in survival of transplanted Luc⁺ allogeneic mGRPs in the CNS. The strategy could be further developed to validate a safe and efficient cell replacement therapy and monitoring for ALS.

References: 1) Srivastava AK, et al. Serial *in vivo* imaging of transplanted allogeneic neural stem cell survival in a mouse model of amyotrophic lateral sclerosis. *Exp Neurol* 2017, 289, 96-102. 2) Kuddannaya, S, et al. In Vivo Imaging of Allografted Glial-Restricted Progenitor Cell Survival and Hydrogel Scaffold Biodegradation. *ACS Appl Mater Interfaces* 2021, 13 (20), 423-437.

Developing CESTheranostics by Enzyme-Mediated Intracellular Self-Assembly of Nanoparticles for Enhanced Imaging and Therapy of Prostate Cancer

Behnaz Ghaemi^a, Aruna Singh^b, Swati Tanwar^c, Yue Yuan^a,
Ishan Barman^c, Michael T. McMahon^b and Jeff W. M. Bulte^{a,b*}

^a*The Russell H. Morgan Department of Radiology and Radiological Science, Division of MR Research, The Johns Hopkins University School of Medicine, Baltimore, MD, USA.*

^b*F.M. Kirby Research Center for Functional Brain Imaging, Kennedy Krieger Inc., Baltimore, MD.*

^c*Department of Mechanical Engineering, Johns Hopkins University, Baltimore, MD.*

Introduction: Metastatic prostate cancer is the most common malignancy affecting men. Treatment strategies for heterogeneous cancers may be revolutionized by using specific tumor enzyme-targeted theranostics. Our overall aim is to develop a precision-based nanotheranostic platform that can be detected by (multi-color) CEST MRI. Taking advantage of enzymatic differences in heterogeneous tumor cells, spheres, and xenograft tumors, we have designed olsalazine-conjugated peptides that can be self-assembled into nanoparticles by the tumor-overexpressed enzymes legumain and/or furin. Olsalazine is a diaCEST MRI contrast agent with a large chemical shift from water protons, and acts as a DNA methylation inhibitor anti-cancer agent.

Methods: Synthesis: R6-AAN-CK peptide was synthesized using solid-phase synthesis followed by conjugation with olsalazine and further conjugated with 2-cyanobenzothiazole (CBT) to create the overall POC complex. Characterization: Matrix-assisted laser desorption ionization (MALDI) and nuclear magnetic resonance (NMR) were used for peptide characterization. In vitro and ex vivo immunohistology: Furin and legumain (over)expression was analyzed in 2D and 3D cell cultures and xenografted tumors. We chose to compare aggressive DU145 prostate adenocarcinoma to less-invasive LNCaP cells and RWPE1 cells healthy cell controls. 3D tumor organoids of prostate cancer were developed and enriched for cancer stem cells up to the 10th generation and their heterogeneity was assessed by evaluating legumain, furin and stemness tumor marker (CD133, CD44 and CD24) expression. In vitro CEST MRI: After incubation of DU145 with 5 mM POC for 3 h, cells were washed and collected for CEST MRI measurement. MRI measurements were performed on a Bruker 11.7 T vertical bore magnetic resonance scanner with a 10-mm birdcage transmit/receive coil.

Discussion: In 2D cultures, the level of legumain and furin expression in DU145 cells far exceeded that of LNCaP and RWPE1 cells. For 3D tumor spheres, legumain was expressed in the periphery while furin was expressed throughout the entire sphere. Both legumain and furin expression increased with each sphere generation. This was accompanied by an increase of cancer stem cells as shown with the CD133⁺, CD44⁺ and CD24⁻ markers. Xenografts also showed heterogeneity in stemness and furin and legumain expression. CEST MRI of DU145 cells exhibited OlsaCEST signal compared to control cells (olsalazine only) as a result of legumain expression, resulting in intracellular accumulation and retention of Olsa¹. We are currently scaling up large batches of furin- and legumain-targeted CESTheranostics for imaging and therapy of heterogeneous prostate cancer in subcutaneous and spontaneous transgenic mouse tumor models.

Conclusion: Our theranostic system with inherent CEST MRI contrast does not require additional labeling that may potentially affect drug distribution. Based on a legumain-mediated CBT click reaction followed by intracellular nanoparticle self-assembly, we successfully developed the POC complex for imaging of tumor aggressiveness, drug accumulation, and therapeutic response in heterogeneous tumors.

References:

1. Yuan, Y.; Zhang, J.; Qi, X.; Li, S.; Liu, G.; Siddhanta, S.; Barman, I.; Song, X.; McMahon, M. T.; Bulte, J. W., Furin-mediated intracellular self-assembly of olsalazine nanoparticles for enhanced magnetic resonance imaging and tumour therapy. *Nature materials* **2019**, *18* (12), 1376-1383.

Development of an MRI agent to detect CD206 and M2-like macrophages

Cuihua Wang^{1,2}, Negin Jalali Motlagh^{1,2}, Gregory R. Wojtkiewicz², John W. Chen^{1,2}

¹Institute for Innovation in Imaging, Department of Radiology, Massachusetts General Hospital, Charlestown, MA 02129; ²Center for Systems Biology, Massachusetts General Hospital and Harvard Medical School, Boston, MA 02114.

Introduction: Two major activated macrophage phenotypes, M1-like and M2-like macrophages, play critical but distinct roles in various pathological conditions. M1-like macrophages produce pro-inflammatory cytokines and other mediators, promote inflammation and cause tissue damage, while M2-like macrophages are anti-inflammatory, reparative and involved in inflammation resolution and tissue repair¹. Manipulation of M1/M2 macrophage balance has emerged as an attractive therapeutic approach. However, understanding of macrophage phenotypes and functions remains challenging because of the heterogeneity and complexity of macrophages in the disease progression as well as the lack of effective tools to interrogate these cells. In this study, we developed a non-invasive MRI method to detect M2-like macrophages by targeting CD206, a marker overexpressed in M2-like activated macrophages.

Methods: *Synthesis:* The CD206-sensing Gd-based MRI agent, MRSP2 and its fluorescent analogue MR-cy5 were synthesized and purified by HPLC. *In vitro validation:* M1 and M2 polarized macrophages differentiated from RAW264.7 cells were incubated with 1 μ M of MR-cy5 at 37 °C for 1 h. The cells were washed and subjected to confocal microscopy. *In vivo imaging.* All animal experiments were approved by and in compliance with the Institutional Animal Care and Use Committee at Massachusetts General Hospital. 8–10-week-old of C57BL/6J and CD206 knock-out mice (Jackson Laboratories) induced with subcutaneous wound healing were used to validate the specificity of MRSP2. We performed MR imaging with serial T1-weighted imaging both before injection and at five time points after the intravenous injection of 0.3 mmol/kg of MRSP2 (15, 30, 45, 60 and 75 mins) on a 4.7-T small animal MR scanner (Bruker, MA) on days 1, 4 and 7 post wound induction.

Results: MRSP2 was synthesized in two steps with a total yield of 32% and MR-cy5 with a yield of 20%. The fluorescence imaging shows that MR-cy5 demonstrated higher binding affinity to M2 macrophages compared to that of M1 macrophages in a cell-based assay (Fig. 1A). For in vivo imaging, the signal over the 75 min time course for wildtype mice was much higher and decreased slower compared to that of CD206 knock-out mice on day 7 after cutaneous injury (Fig. 1B and 1C), demonstrating that MRSP2 is responsive and specific to CD206. Longitudinal imaging shows that signal at 60 min on day 4 was much lower and decreased faster than that on days 1 and 7 (Fig. 1C) in wildtype mice, concordant with the increased M2-like macrophages in the reparative stage of wound healing (day 7) than that in the early inflammatory stage (day 4) when the M1-like macrophages are dominant².

Discussion: CD206 recognizes and binds to terminal mannose, fucose or N-acetylglucosamine through carbohydrate-recognition domains and is expressed at elevated levels in M2-like cells in various pathological conditions. Both in vitro binding affinity assay and in vivo imaging in mice with cutaneous injury from this study confirm the specificity of MRSP2 to CD206 and its capacity to detect M2-like macrophages.

Conclusion: MR imaging of MRSP2 is capable of tracking the changes of M2-like macrophages in the procession of pathologies. In the near future, we will be applying this imaging technology to study inflammatory diseases in which M2-like macrophages play important roles.

References:

1) Mantovani, A., et al., *Macrophage plasticity and polarization in tissue repair and remodelling*. J Pathol, 2013. **229** (2): p. 176-85. 2) Koh, T.J. and L.A. DiPietro, *Inflammation and wound healing: the role of the macrophage*. Expert Rev Mol Med, 2011. **13**: p. e23.

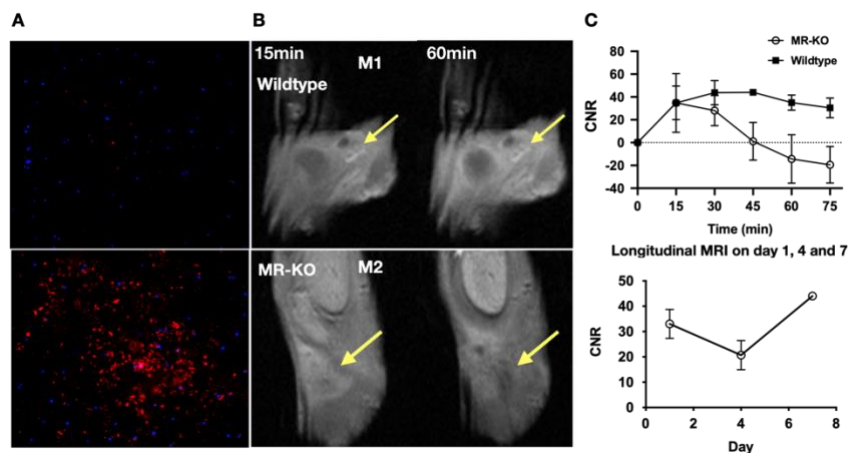


Figure 1. A) In vitro validation shows higher binding affinity of MR-cy5 to M2 macrophages than that to M1 macrophage (Blue, DAPI; Red, MR-cy5). B) Representative MR images of wildtype and CD206 knock-out mice in a model of subcutaneous wound healing. C) Contrast-to-noise ratios (CNRs) over 75 min and longitudinal imaging on days 1, 4 and 7 (n = 3 for each group).

High-Contrast-Ratio Tunable and Switchable MRI Labels using Magnetocaloric Materials

Mladen Barbic¹, Stephen Dodd², and Alan P. Koretsky²

¹NYU Langone Health – Tech4Health Institute, New York, NY, United States, ²NIH/NINDS, Bethesda, MD, United States

Introduction: Development of novel contrast mechanisms and labeling agents for MRI is critical for further advancements in non-invasive cell imaging, tracking, and readout of physiological conditions in-vivo¹⁻³. Recent advances in magneto-caloric materials provide an opportunity to apply these materials as tunable and switchable contrast agents for MRI. More specifically, the extremely sharp first-order magnetic phase transitions these materials have (with both positive and negative magnetization vs temperature slopes) at typical physiological temperatures and in the presence of the large DC magnetic field values associated with MRI scanners provide an ideal match to the requirements for the design of novel MRI labels⁴⁻⁶.

Methods: *Synthesis:* Magnetocaloric Lanthanum-Iron-Silicon (La-Fe-Si) powder sample (100-250 μ m particle size) was obtained from a commercial vendor (Vacuumschmelzte Calorivach). Magnetocaloric Iron-Rhodium (FeRh) granules (Fe 49%, Rh 51% atomic composition) were prepared by mixing in an arc melting furnace (American Elements Corp.), followed by high-temperature annealing in Argon gas furnace at 1,000 $^{\circ}$ C for two weeks, and subsequently quenched in ice-water. *Magnetic Characterization:* Temperature and field dependent magnetic measurements were performed in a vibrating sample magnetometer (Quantum Design, Inc.). *Temperature dependent MRI:* 1T system (ICON) was used, as that was the available polarizing MRI DC magnetic field that was closest to the value where the sharp first order transition happens near the physiological temperature of 37 $^{\circ}$ C (310K). The samples were embedded in agarose next to a MRI-compatible optical fiber based thermometer (FISO Technologies, Inc.). The sample tube was wrapped in water

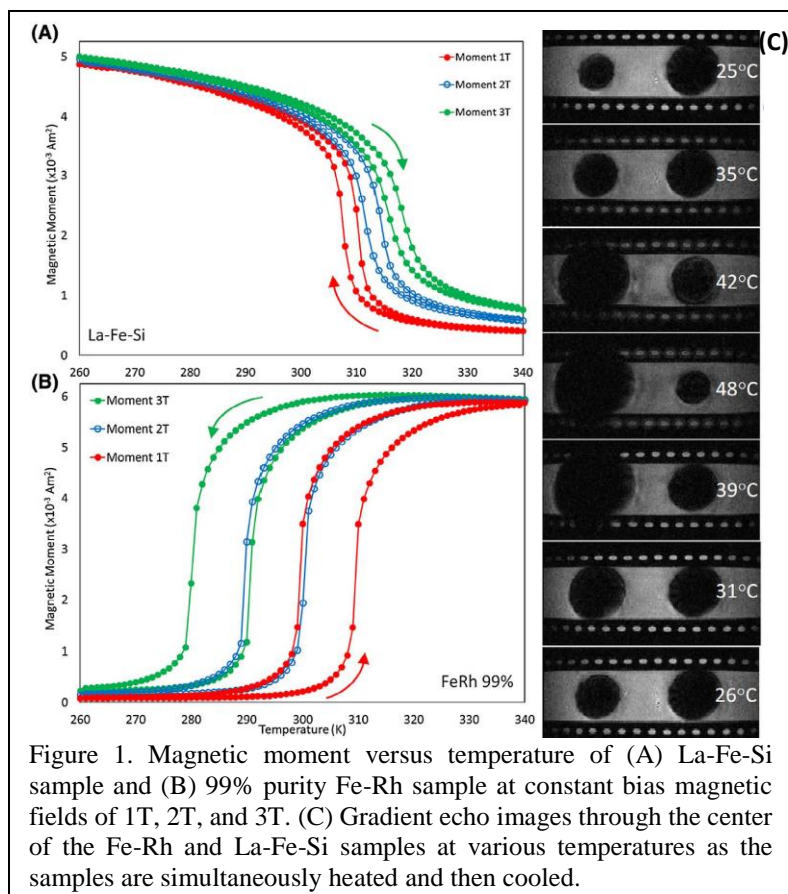


Figure 1. Magnetic moment versus temperature of (A) La-Fe-Si sample and (B) 99% purity Fe-Rh sample at constant bias magnetic fields of 1T, 2T, and 3T. (C) Gradient echo images through the center of the Fe-Rh and La-Fe-Si samples at various temperatures as the samples are simultaneously heated and then cooled.

tubing connected to a temperature controlled water circulating bath in order to sweep and control the temperature of the sample and its environment around physiologically relevant conditions. **Results:** Figures 1A-B show magnetic moment vs. temperature measurements at three constant DC fields (1T, 2T and 3T) as the temperature is swept. Both materials have sharp first order magnetic phase transitions, but with opposite slopes. At 1T (red curves) the magnetic phase transition for both materials is at the same physiological temperature. Figure 1C shows a sequence of gradient-echo images of the Fe-Rh and La-Fe-Si samples at various temperatures as the two samples are simultaneously heated and then cooled. In Figure 2, MRI contrast dependence is shown in the gradient echo images for 100 μ m diameter La-Fe-Rh particles at 1T as the temperature is swept. In another set of experiments, MRI-compatible focused ultrasound (FUS) was used⁶ for

selective fast focal switching of magnetocaloric MRI particles at 1.5T. Overall, high MRI contrast ratio switching was demonstrated in 1T, 1.5T, 4.7T, and 7T scanners with different magnetocaloric materials⁴⁻⁶. **Discussion and Conclusion:** The results clearly demonstrate significant contrast changes in the MRI due to the sharp first order phase transition of magnetocaloric materials in Tesla-scale fields and at physiological temperatures. Such demonstrations provide the impetus for utilizing these materials for cell tracking and other applications where high differential contrast ratio would be beneficial such as catheter localization.

References: 1. Bulte JWM, Kraitchman DL. Iron oxide MR contrast agents for molecular and cellular imaging. *NMR Biomed.* 2004; **17**: 484-499. 2. Shapiro EM, et al. MRI detection of single particles for cellular imaging. *Proc. Natl. Acad. Sci. USA.* 2004; **101**: 10901-10906. 3. Ahrens ET, Bulte JW. Tracking immune cells in vivo using magnetic resonance imaging. *Nat. Rev. Immunol.* 2013; **13**: 755-763. 4. M. Barbic, et al, "Magnetocaloric Materials as Switchable High Contrast Ratio MRI Labels" *Mag. Res. Med.* **81**, 2238 (2019). 5. M. Barbic, et al, "Multifield and Inverse-Contrast Switching of Magnetocaloric High Contrast Ratio MRI Labels" *Mag. Res. Med.* **85**, 506 (2021). 6. G. W. Miller, et al, "Selective fast focal switching of high-contrast-ratio magnetocaloric MRI labels with focused ultrasound" *Proc. Intl. Soc. Mag. Reson. Med.* **28**, 4119 (2020).

selective fast focal switching of magnetocaloric MRI particles at 1.5T. Overall, high MRI contrast ratio switching was demonstrated in 1T, 1.5T, 4.7T, and 7T scanners with different magnetocaloric materials⁴⁻⁶.

Discussion and Conclusion: The results clearly demonstrate significant contrast changes in the MRI due to the sharp first order phase transition of magnetocaloric materials in Tesla-scale fields and at physiological temperatures. Such demonstrations provide the impetus for utilizing these materials for cell tracking and other applications where high differential contrast ratio would be beneficial such as catheter localization.

References: 1. Bulte JWM, Kraitchman DL. Iron oxide MR contrast agents for molecular and cellular imaging. *NMR Biomed.* 2004; **17**: 484-499. 2. Shapiro EM, et al. MRI detection of single particles for cellular imaging. *Proc. Natl. Acad. Sci. USA.* 2004; **101**: 10901-10906. 3. Ahrens ET, Bulte JW. Tracking immune cells in vivo using magnetic resonance imaging. *Nat. Rev. Immunol.* 2013; **13**: 755-763. 4. M. Barbic, et al, "Magnetocaloric Materials as Switchable High Contrast Ratio MRI Labels" *Mag. Res. Med.* **81**, 2238 (2019). 5. M. Barbic, et al, "Multifield and Inverse-Contrast Switching of Magnetocaloric High Contrast Ratio MRI Labels" *Mag. Res. Med.* **85**, 506 (2021). 6. G. W. Miller, et al, "Selective fast focal switching of high-contrast-ratio magnetocaloric MRI labels with focused ultrasound" *Proc. Intl. Soc. Mag. Reson. Med.* **28**, 4119 (2020).

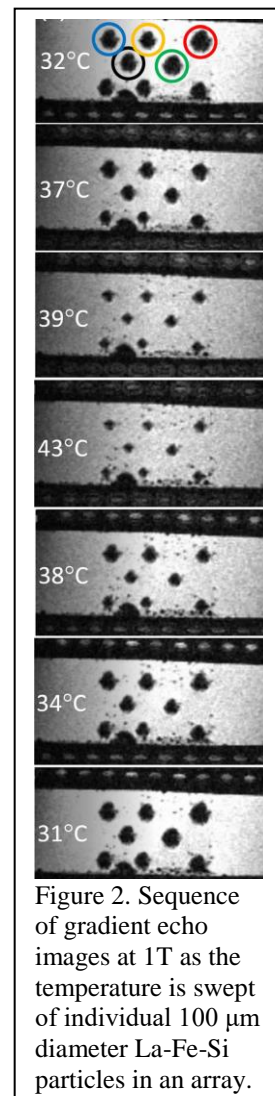


Figure 2. Sequence of gradient echo images at 1T as the temperature is swept of individual 100 μ m diameter La-Fe-Si particles in an array.

Using synthetic notch to visualize cell-cell communication in vivo with magnetic resonance imaging

TianDuo Wang^{1,2}, Yuanxin Chen¹, Nivin Nystrom^{1,2}, Shirley Liu^{1,2}, John. A. Ronald^{1,2,3}

1. Robarts Research Institute – Imaging; 2. Department of Medical Biophysics, University of Western Ontario;

3. Lawson Health Research Institute, London, ON, Canada.

Introduction: Cellular therapies rely on proper communication between delivered cells and their target. Cellular immunotherapies harness the innate tumour-homing ability of immune cells to better target and kill malignant cells. To improve cancer killing, immune cells can be engineered with targeting receptors, such as chimeric antigen receptors (CAR)¹, to recognize specific cancer antigens. CAR-T cells have already shown remarkable clinical success in treating B-cell cancers, with potential to treat other cancer types on the horizon. However, some patients still suffer from inadequate efficacy and/or serious side effects, thought to be due to sub-optimal tumour-homing and off-targeting of normal tissues by immune cells. This study aims to develop a non-invasive and clinically-relevant imaging tool to visualize when immune cells interact with its targeted antigen – the prerequisite for inducing cancer killing. The synthetic notch (SynNotch) receptor is a uniquely versatile system that signals cell-cell contact via activatable transcriptional expression of desired transgenes² (Fig. 1A). In this work, we engineered immune cells with a SynNotch system that activates the expression of multimodal imaging reporter genes in response to cancer antigen binding.

Methods: We engineered a human T cell line (Jurkat) via lentiviral transduction of two components: (1) SynNotch receptor directed against the B-cell surface antigen CD19³, and (2) a response element containing tdTomato (tdT) for fluorescence, firefly luciferase (Fluc) for bioluminescence (BLI), and organic anion transporting polypeptide 1B3 (OATP1B3) for MRI⁴. Successfully engineered T cells were isolated using fluorescence activated cell sorting. For *in vivo* evaluation, Nod-scid-gamma mice were implanted with either CD19+ or CD19- Nalm6 leukemia cells subcutaneously. Once tumours reached >100mm³, mice received an intratumoural injection of 10 million engineered T cells. BLI and gadolinium-enhanced T₁-weighted MRI was performed to assess Fluc and OATP1B3 reporter activation in tumours, respectively. Contrast-to-noise ratio (CNR) measurements were performed by a blinded observer by drawing regions representing the enhanced cells and tumour background on individual slices and averaged per mouse.

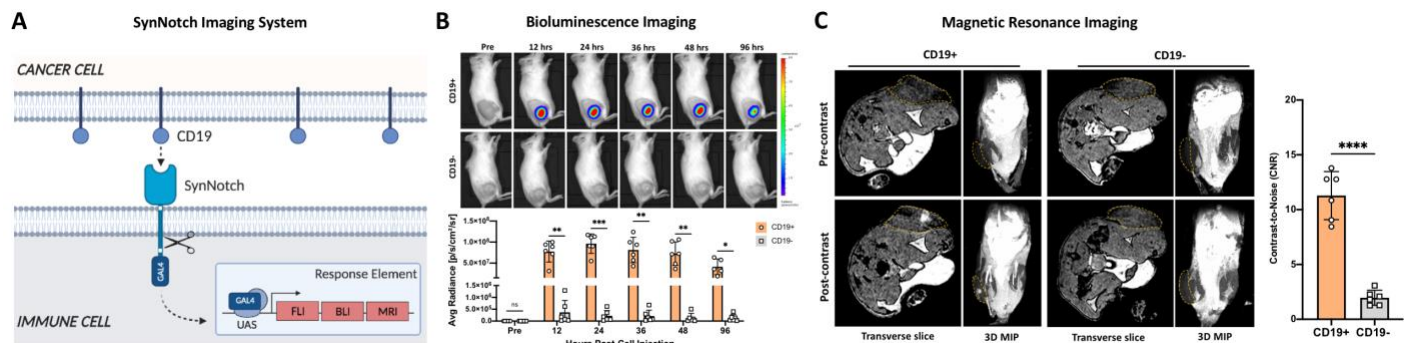


Figure 1. (A) Schematic of SynNotch system. CD19 binding induces intracellular cleavage of a GAL4-VP64 transactivator, which binds to an upstream activating sequence (UAS) to initiate transcription of encoded reporter genes. (B) Representative bioluminescence images with quantification of Fluc signal in subcutaneous tumours pre- and post-cell injection (N=6). (C) T₁-weighted MRI pre- and 5 hours post-contrast with Primovist gadolinium agent. Tumours are outlined on transverse slices and 3D maximal intensity projections (N=6). Average CNR of enhanced regions compared to tumour background is provided.

Results: BLI revealed minimal background Fluc activity in subcutaneous tumours prior to T cell injection (Fig. 1C). Excitingly, as early as 12 hours post-intratumoural T cell injection, mice carrying CD19+ tumours showed significantly elevated Fluc signal compared to mice with CD19- tumours at all timepoints. Following administration of the gadolinium agent Primovist, MRI revealed notable regions of contrast enhancement in CD19+ tumours (Fig 2C). These enhanced regions in CD19+ tumours exhibited significantly higher contrast-to-noise over the tumour background compared to CD19- tumours.

Discussion: In this work, we have demonstrated the selective activation of reporter genes in immune cells interacting with cancer cells in an antigen-dependent manner with minimal off-target activity. Notably, using MRI, we visualized discernable regions of localized enhancement within CD19+ tumours, but not CD19- tumours, reflective of activatable OATP1B3 expression in T cells. Next steps for this work include adapting this system for other immune cell types like natural killer (NK) cells and engineered cells like CAR-T cells. Moreover, the modularity the SynNotch system allows us to target antigens expressed by solid tumours, and we are currently exploring our system with multiple cancer types. We posit these tools will ultimately improve our ability to develop better cell products and to understand response/non-response and side effects in individual patients.

Conclusion: Here we have developed a molecular imaging system to visualize antigen-specific communication between cells *in vivo* for the first time – notably visualizing cell interactions via a human-derived, clinically-relevant MR reporter. Further development of this technology will provide an imaging tool which could improve our ability to understand and monitor cell-cell interactions in multicellular organisms, which could be broadly applicable for therapeutics, diagnostics, and beyond.

References: [1] Maude et al., *NEJM*, 2014, 371: 1507-1517. [2] Morsut et al., *Cell*, 2016, 164: 780-791. [3] Sadelain et al., *J Clin Invest*, 2015, 125(9): 3392-3400. [4] Nystrom et al., *Invest Radiol*, 2019, 54(5): 302-311.

Multiparametric MRI for tissue classification of subcutaneous MC38 colon cancer using oxygen enhanced, dynamic contrast enhancement (DCE) MRI and [¹⁸F]FAZA PET.

Marta Vuozzo^{1,2}, Max Zimmermann¹, Remy Chiaffarelli¹, Stefania Pezzana¹, Bernd J. Pichler^{1,2} and Andreas M. Schmid^{1,2}

¹ Werner Siemens Imaging Center, Department of Preclinical Imaging and Radiopharmacy, University Hospital Tuebingen, Tuebingen, Germany. ² Cluster of Excellence iFIT (EXC 2180) "Image-Guided and Functionally Instructed Tumor Therapies", University of Tübingen, Germany.

Introduction: Hypoxia is a common feature of malignant tumours, and is a potential prognostic biomarker for tumor aggressiveness, progression, and response to therapy. Hence, a method for imaging tumor oxygenation and perfusion is of utmost importance, even more as immunotherapy follow-up. Previous reports showed a direct correlation between oxygen sensitive MRI and PET hypoxia reporter agents in the rat prostate tumors¹. Here, we use multiparametric MRI including T1-, T2s mapping, dynamic contrast enhanced MRI and oxygen-level dependent contrast to characterize tumor and muscle tissue. Subsequently, supervised (neural network-based) and unsupervised (k-means, Gaussian Mixture Models, GMM) clustering methods are applied and clustering accuracy is assessed. **Methods:** Seven C57BL/6 mice were injected subcutaneously with 5×10^5 MC38 tumor cells. One week after cell injection, mice received PDL1 monotherapy for 3 consecutive weeks. We performed blood oxygen level dependent (BOLD) and tissue oxygen level dependent (TOLD) MRI while applying a 100% oxygen gas breathing challenge, followed by a Gd-based DCE assessment of perfusion. For comparison a static PET was performed 120 minutes after i.v. injection of [¹⁸F]FAZA. Multiparametric maps, including T1 pre-, post- oxygen and post-Gd, T2* pre- and post-oxygen, wash-in maps obtained from T1 dynamic, T2* dynamic during oxygen challenge and from DCE MRI, were calculated using MatLab. Coregistration of MRI and PET data assured accurate characterization of individual voxels from PET and MRI. **Results:** The analysis pipeline for voxelbased characterization of tissue using >10 different imaging protocols was successfully setup. Tumor volumes varied strongly between responders ($14.5 \pm 23.3 \text{ mm}^3$) and non-responders ($548.2 \pm 217.8 \text{ mm}^3$) at the endpoint of the study. Our preliminary cluster analysis showed higher stability of CNN-clustered data compared to the unsupervised methods. **Discussion:** Tumor growth in our small cohort of animals was in accordance to literature and previous experience. The major limitation of our study was the restricted sample size, which so far did not allow a specific validation study. Further, in depth segmentation of the tumors was impaired by the strong difference in tumor growth between responding and resistant tumors. **Conclusion:** The strong biological difference within the treatment group is a great challenge to data analysis. While manual data analysis mostly relies on tumor growth, our indepth characterization of the different tumor tissues can play a major role in detecting therapy responders early. However, further investigations are needed to successfully differentiate responders and non-responders in this tumor model.

References: [1] Zhou H, Chiguru S, Hallac RR, Yang D, Hao G, Peschke P, Mason RP. Examining correlations of oxygen sensitive MRI (BOLD/TOLD) with [¹⁸F]FMISO PET in rat prostate tumors. Am J Nucl Med Mol Imaging. 2019 Apr 15;9(2):156-167. PMID: 31139498; PMCID: PMC6526364.

Mn²⁺-bispidines: a novel platform for Mn²⁺-based MRI agents

D. Ndiaye,¹ M. Sy,² A. Nonat,² L. Charbonnière,² P. Cieslik,³ P. Comba,³ E. Toth¹

1. Centre of Molecular Biophysics, CNRS, Orléans, France; 2. IPHC Strasbourg, France, 3. Univ. of Heidelberg, Germany

eva.jakabtoth@cnrs-orleans.fr

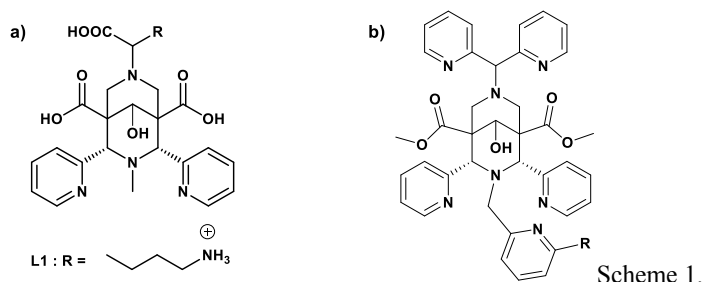
Introduction: The search for more biocompatible alternatives to Gd³⁺-based MRI agents calls for ligands that form stable and inert Mn²⁺ chelates. The lower charge (with respect to Gd³⁺) and the lack of ligand-field stabilization energy for the high-spin d⁵ electron configuration are not favorable to achieve high thermodynamic stability; the highly labile nature of Mn²⁺ sets an even more difficult challenge to meet.

Methods: We have investigated a series of bispidine chelators for Mn²⁺ complexation. Bispidine-type ligands represent a versatile platform in coordination chemistry. We hypothesized that the very rigid scaffold of 2,4-pyridyl-disubstituted bispidol derivatives bearing one methylene carboxylic acid (Scheme 1a) can endow Mn²⁺ chelates with high kinetic inertness, while maintaining good relaxation properties due to the presence of hydration water. Another bispidine family (Scheme 1b) has been designed to achieve high selectivity for Mn²⁺ over the endogenous competitor Zn²⁺. A preference for Mn²⁺ over the other first row transition metal di-cations requires a large and rigid cavity – depending on the coordination number, the size of Mn²⁺ is approx. 10% larger than that of Zn²⁺. The relatively large cavity imposed by a high denticity of an open-chained ligand may enforce one of the pendant donor groups to be uncoordinated with the smaller competitor Zn²⁺. The Mn²⁺ complexes have been characterized with respect to thermodynamic stability, kinetic inertness, relaxation properties and in vivo MR imaging capabilities.

Results and discussion: the MnL₁ complex has an exceptional resistance to dissociation. At 37°C, pH 6 and in the presence of up to 50 equivalents of Zn²⁺, MnL₁ remained intact for at least 140 days. These complexes have higher proton relaxivities than most monohydrated, small molecular weight Mn²⁺ chelates, which might be related to a second sphere relaxivity contribution induced by the non-coordinating carboxylates functions. *In vivo* MRI experiments performed in mice indicate quick renal clearance.

Stability and structural data determined for the second family (Scheme 1b) confirm that the rigid and large bispidine scaffold and the pendant donors perfectly wrap around the Mn²⁺ ion, leading to record stabilities. Most importantly, we observe unprecedented selectivity for Mn²⁺ vs. Zn²⁺, amounting to over 9 log*K* units. These ligands represent the first examples of real and efficient Mn²⁺ selectivity in aqueous solution. Relaxation properties are also interesting, allowing for efficient MR contrast enhancement in mice.

Conclusion: Bispidine ligands constitute a very promising platform to develop non-specific, as well as targeted and responsive Mn²⁺-based agents.^{1,2}



1. D. Ndiaye, M. Sy, A. Pallier, S. Mème, I. de Silva, S. Lacerda, A. M. Nonat, L. J. Charbonnière and É. Tóth, *Angew. Chem. Int. Ed.* **2020**, *59*, 11958-11963.
2. P. Cieslik, P. Comba, B. Dittmar, D. Ndiaye, É. Tóth, G. Velmurugan, H. Wadepohl, *Angew. Chem. Int. Ed.* **2022**, accepted, doi.org/10.1002/anie.202115580

Non-invasive Imaging of β -Cell Function in the Rat Pancreas by use of a Zinc-Responsive MRI Contrast Agent

Eul Hyun Suh¹, Bibek Thapa¹, Daniel Parrott^{1,2}, Pooyan Khalighinejad¹, Gaurav Sharma¹, Sara Chirayil¹, and A. Dean Sherry^{1,2,3}

¹Advanced Imaging Research Center, UT Southwestern Medical Center, Dallas, Texas, United States, ²Department of Radiology, UT Southwestern Medical Center, Dallas, Texas, United States, ³Department of Chemistry, UT Dallas, Texas, United States.

Introduction: Regulated glucose-stimulated insulin secretion (GSIS) by pancreatic β -cell function plays a key role in maintaining blood glucose homeostasis and it is impaired in diabetes mellitus, particularly in type 2 diabetes¹. An imaging method for detecting β -cell function in real-time could provide new insights into the biological mechanisms involving loss of β -cell function during development of type 2 diabetes and for testing of new drugs designed to modulate insulin secretion. In this study, we used gadolinium-based zinc-responsive agent (GdL2) and an optimized 2D-MRI method to show that glucose stimulated insulin and zinc secretion (GSZS) can be detected as functionally active “hot spots” in the tail of pancreas².

Methods: In vivo imaging: All animal experiments were performed in accordance with guidelines by the institute IACUC committee. MRI was performed in a 9.4 T Varian preclinical scanner with 72 mm volume coil using Gd-based Zn²⁺ sensors, GdL2 prepared as described previously³ to provide a direct way to imaging β -cell function. A total of 24 rats (male, 11–14 weeks age; Sprague Dawley #400) were used for *in vivo* MR imaging experiments. The rats were fasted overnight before imaging. 6 rats were imaged after tail vein injection of GdL2 plus saline, 6 rats were imaged after injection of GdL2 plus glucose 6 rats were used in the STZ-treated group and 6 rats were imaged after injection of GdL2 plus glucose plus exenatide. The dosage of glucose was 2.75 mmol/kg dissolved in 0.9% normal saline (0.5 g/L solution) and 0.9% normal saline alone was injected followed by 0.1 mmol/kg GdL2. Immediately after injection, a series of gradient echo 2D multi-slice (TE/TR 4.27/129.81ms, matrix 256x256) were obtained to observe the dynamic glucose response and Zn²⁺ release in pancreas. **Co-Registration of Ex Vivo MRI With Histology:** The pancreas was excised completely after injection of GdL2 plus glucose as described above then imaged by MRI using identical parameter as used *in vivo*. The pancreas was fixed in 10% paraformaldehyde for insulin-specific immunohistochemical and H&E staining.

Results: We observed that GdL2 can non-invasively detect Zn²⁺ secretion from β -cells during glucose-stimulated insulin secretion (GSIS) *in vivo* as high intensity, focal “hot spots” in the pancreatic tail (Figure 1A). The injection of GdL2 plus glucose resulted in substantially higher signal enhancement in the pancreatic tail ($77 \pm 2.1\%$ p < 0.0001) unlikely saline control group (Figure 1A,B). Co-registration of MRI detected hot spots with immunohistochemical staining for insulin were conducted to confirm that the observed “hot spots” correspond to islets. (Figure 1 C-E). By immediately fixing the pancreas after *ex vivo* MR imaging, the almost close location of hot spots (Zn²⁺ secretion), insulin (islets), and blood vessels (H&E) could be displayed in nearly identical anatomic planes. The pharmacological interventions demonstrated the MRI hot spots reflect islet functions in a group of Sprague-Dawley rats treated with streptozotocin (STZ) and exenatide.

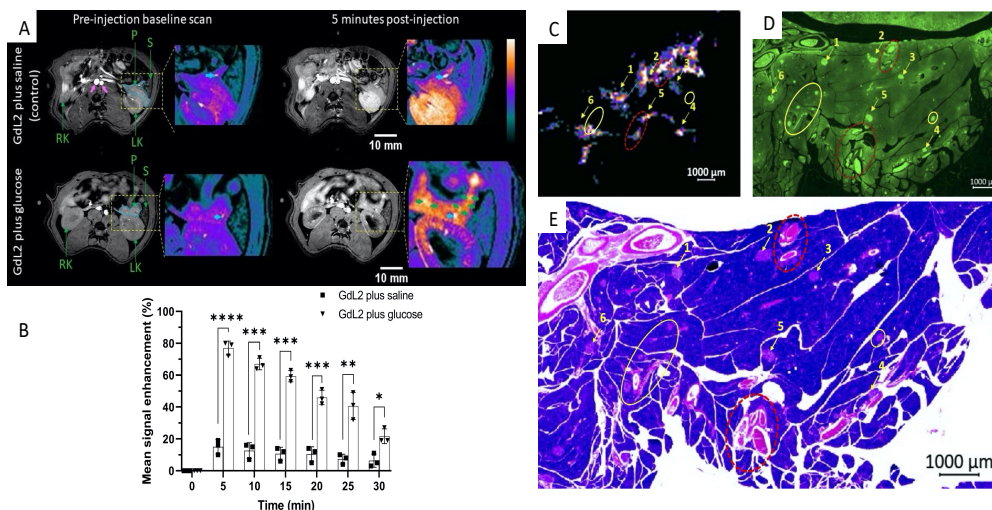


Figure 1. (A) Axial T1-weighted pre- and 5 min post-contrast MRI of rat pancreas after administration of GdL2 plus saline (top row) or GdL2 plus glucose (bottom row). The pancreas is outlined with solid cyan in pre-contrast images. (B) Pancreas signal enhancement over time in rats injected with either GdL2 plus glucose or GdL2 plus saline shown as the mean \pm SD. (C) MR signals detected in an *ex vivo* pancreas removed from a rat 5 min after injection of GdL2 plus glucose. (D) Islets identified by immunofluorescence staining for insulin and (E) H&E. Note that some hot spots observed by MRI reflect blood vessels (red dotted circles), respectively. Interestingly, some insulin-stained islets do not appear as hot spots in the MR image shown in (C) (yellow circles).

Conclusions: This imaging method will be useful for monitoring the efficacy of new drugs designed to stimulate β -cell function and, given that it is non-invasive and allows for longitudinal studies, for monitoring progressive loss of β -cell function during development of type 2 diabetes in rodents.

References: 1) Harcourt, B.E., *et al.* Coming full circle in diabetes mellitus: from complications to initiation. *Nat Rev Endocrinol* 9,113-123 (2013). 2) Thapa, B., *et al.* Imaging β -Cell Function Using a Zinc-Responsive MRI Contrast Agent May Identify First Responder Islets. *Frontiers in Endocrinology* 12(2022). 3) Martins, A.F., *et al.* Imaging Insulin Secretion from Mouse Pancreas by MRI Is Improved by Use of a Zinc-Responsive MRI Sensor with Lower Affinity for Zn²⁺ Ions. *J Am Chem Soc* 140, 17456-17464 (2018).

Discussion: Given that GdL2 likely does not enter cells, the higher signal enhancement observed after injection of glucose can only be attributed to release of Zn²⁺ ions from islet β -cells. Freely available extracellular Zn²⁺ by glucose stimulation rapidly binds the side-arms of GdL2 to form of GdL2-Zn²⁺-albumin ternary complex, an increase in r_1 , and subsequently image contrast enhancement. A comparison of functional images with histological markers show that insulin and zinc secretion does not occur uniformly among all pancreatic islets but some islets respond rapidly to an increase in glucose while others remain silent. Zinc and insulin secretion was shown to be altered in streptozotocin and exenatide treated rats thereby verifying that this MRI technique is responsive to changes in β -cell functions.

Imaging immune cells with fluorine-19 MRI

Olivia C. Sehl^{1,2}, Corby Fink^{1,3}, Katherine MacDonald⁴, Veronica P. Dubois^{1,2}, Marina Ninkov³, Mansour Haeryfar³, John A. Ronald^{1,2}, Megan Levings^{4,5}, Greg A. Dekaban^{1,3}, Paula J. Foster^{1,2}

¹Robarts Research Institute, London, ON, ²Department of Medical Biophysics, Western University, London, ON, ³Department of Microbiology and Immunology, Western University, London, ON, ⁴School of Biomedical Engineering, The University of British Columbia, BC Children's Hospital Research Institute, Vancouver, BC, ⁵Department of Surgery, The University of British Columbia, Vancouver, BC

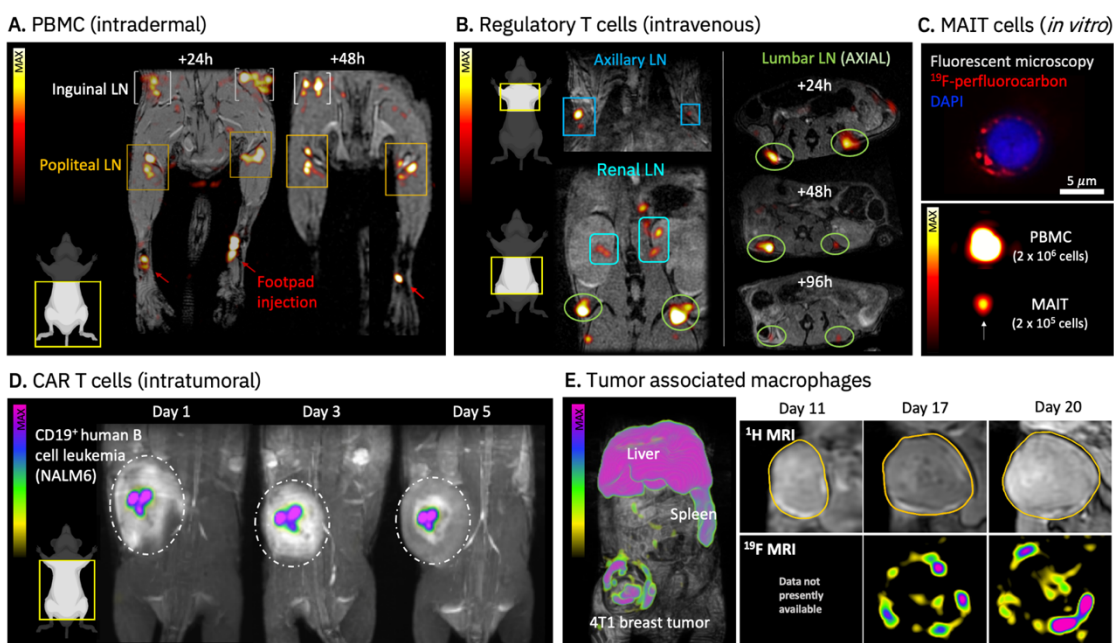
Rationale: Several cell-based cancer immunotherapies have been approved in recent years, for example, peripheral blood mononuclear cells (PBMC) for prostate cancer (Provenge®)^{1,2} and chimeric antigen receptor (CAR) T cells for leukemia, lymphoma, and myeloma (Yescarta®, Tescarta®, Kymriah®, Abecma®, Carvykti®)³. To be effective, therapeutic cells must migrate to target site(s), including secondary lymphoid tissues or tumors, and in sufficient numbers⁴. A major challenge is the inability to monitor the movement and persistence of these cells after administration. Some immunotherapy approaches also consider tumor-associated macrophages (TAMs) as a target^{5,6}. TAMs are abundant and influential cells in the dynamic tumor microenvironment that promote tumor growth, progression, and metastasis^{7,8}. Current investigations of TAMs using histology are limited to only a portion of a tumor and a single timepoint.

Imaging has the potential to revolutionize our ability to monitor cell therapies and TAMs and provide a full picture that can be used to optimize immunotherapeutic strategies. Fluorine-19 (¹⁹F) magnetic resonance imaging (MRI) is a clinically applicable technique that can be used to directly detect and quantify ¹⁹F-labeled cells⁴. The resulting hotspot images contain signal which is directly proportional to the number of cells present, in the absence of any appreciable background signal⁹. Here we demonstrate ¹⁹F MRI tracking of (A) PBMC¹⁰, (B) regulatory T cells (Tregs), (C) mucosal-associated invariant T (MAIT) cells, (D) CAR T cells¹¹, and (E) TAMs, which were detected in mice at multiple timepoints and target locations.

Methods: Human PBMC, Treg, MAIT, and CAR T cells were pre-labeled with ¹⁹F in culture prior to their administration to immunocompromised mice. This was achieved through overnight coincubation with clinical grade ¹⁹F-perfluorocarbons (CS-1000, Celsense Inc.). TAMs in 4T1 tumors were labeled by intravenous administration of ¹⁹F-perfluorocarbons (VS-1000H, Celsense Inc.) 24 hours prior to imaging. Mouse imaging was conducted on a 3 Tesla human MRI system and a 4.3 cm diameter dual-tuned (¹H/¹⁹F) surface coil was used to acquire ¹H and ¹⁹F images in the same field of view¹². A sensitive bSSFP pulse sequence was used and ¹⁹F images were acquired in 35 minutes or less.

Results/Discussion: ¹⁹F MRI cell tracking with clinically applicable methodology is widely feasible for a variety of immune cell types. Following administration, (A) PBMC and (B) Treg were detected in LN and (D) CAR T cells persisted in leukemia tumors. ¹⁹F quantification revealed fewer cells were present *in vivo* over time. (C) MAIT cell labeling with ¹⁹F-perfluorocarbon was successful as shown with fluorescent microscopy and ¹⁹F imaging of MAIT cell pellets. (E) ¹⁹F-labeled TAMs were detected predominately at the periphery of 4T1 tumors and increased ¹⁹F signal is detected at later timepoints, indicating the number of TAMs increase as tumors grow. ¹⁹F signals also detected in normal tissues that are naturally macrophage rich, including the spleen and liver.

Significance: This is the first demonstration of Treg and MAIT cell tracking with ¹⁹F MRI, and the first time PBMC and CAR T cells were imaged using clinical magnetic field strengths (3T). Importantly, imaging these cells at 3T improves the clinical translation of ¹⁹F MRI.



[1] Bulte, J.W.M. & Shakeri-Zadeh, A. *MIB* 1-10 (2021). [2] Fink, C. *et al. Sci. Rep.* 8, 1-13 (2018). [3] Martinez, M. & Moon, E.K. *Front. Immunol.* 10, 1-21 (2019). [4] Ahrens, E.T., *et al. MRM* 72, 1696-1701 (2014). [5] De Palma, M. & Lewis, C.E. *Cancer Cell* 23, 277-286 (2013). [6] Guerriero J.L. *Trends Mol. Med.* 24, 472-489 (2018). [7] Gwak, J.M. *et al. PLoS One* (2015). [8] Sørensen, M.D. *et al. Neuropathol. Appl. Neurobiol.* 44, 185-206 (2018). [9] Chapelin, F. *et al. Immunother. Cancer* 8, 1-10 (2018). [10] Fink, C. *et al. Diagn. Interv. Imaging* (2020). [11] Dubois, V.P. *et al. MIB* (2021). [12] Makela, A.V. & Foster, P.J. *MAGMA* (2018).

Towards fully biocompatible PHIP polarized pyruvate for in-vivo metabolic investigations

Francesca Reineri,¹ Oksana Bondar,¹ Carla Carrera² and Silvio Aime¹

¹Torino University, Dept. Molecular Biotechnology and Health Sciences, Via Nizza 52, Torino, Italy

²Institute of Biostructures and Bioimaging National Research Council Via Nizza 52, 10126 Torino (Italy)

Introduction

Hyperpolarized pyruvate is the metabolite that has been most widely applied into metabolic investigations, and the first HP compound that has been translated into clinical studies. The gold-standard hyperpolarization method d-DNP (dissolution-Dynamic Nuclear Polarization) can provide doses of this highly polarized and concentrated metabolite, but the applications are limited by the costs of instrumentation and maintenance, technical difficulties and long polarization cycles. ParaHydrogen Induced Polarization and Side Arm Hydrogenation [1] allows to produce HP of [1-¹³C]pyruvate, and other molecules containing a terminal carboxylate group [2], but a few issues, concerning the hyperpolarization level and the presence of residual traces of the metal catalyst in the final solution.

Methods

Propargyl-[1-¹³C] pyruvate was hydrogenated, using parahydrogen, in an organic, hydrophobic solvent. The concentration of the metal catalyst, used for hydrogenation, has been significantly reduced, with respect to that previously used, thanks to the addition of a phosphine ligand in the hydrogenation mixture.

Spin order transfer from the parahydrogen protons to the ¹³C carboxylate spin has been carried out by means of magnetic field cycling and cleavage of the ester has been obtained using an aqueous base solution (NaOH 0.1M). The hyperpolarized metabolite is extracted in the water phase, while the catalyst is retained in the organic one, and the two phases separate in few seconds. An acidic buffer (HEPES) is added to the aqueous phase, in order to reach physiological pH, the aqueous solution is, then, filtered through a lipophilic resin (TENAX® TA porous polymer adsorbent), collected in a syringe for MRI in-vitro and in-vivo.

¹³C-MRS and ¹³C-csi experiments have been acquired on a 3T-MRI Bruker Biospect and on a 7T-MRI.

Results and discussion

The aqueous solution of hyperpolarized [1-¹³C]pyruvate, before filtration through the lipophilic resin, contains non-neglectable concentrations of the organic solvents (chloroform and toluene) used to carry out the parahydrogenation reaction. Cytotoxicity studies on tumor cells showed a toxicity effect associated with the presence of the organic solvent (chloroform). Filtration through the resin allows to remove the solvents almost completely,[3] and the concentration of these solvents is lower than those recommended by the EPA (Environmental Protection Agency). The concentration of the metal in the final aqueous solution is also significantly lower (~1 uM) than the previously reported one (~30uM), thanks to the lower catalyst concentration used in the hydrogenation step.

In the *in vivo* experiments (figure 1) ¹³C-csi clearly shows the signals from HP 1-¹³C lactate derived from metabolism of HP [1-¹³C]pyruvate.

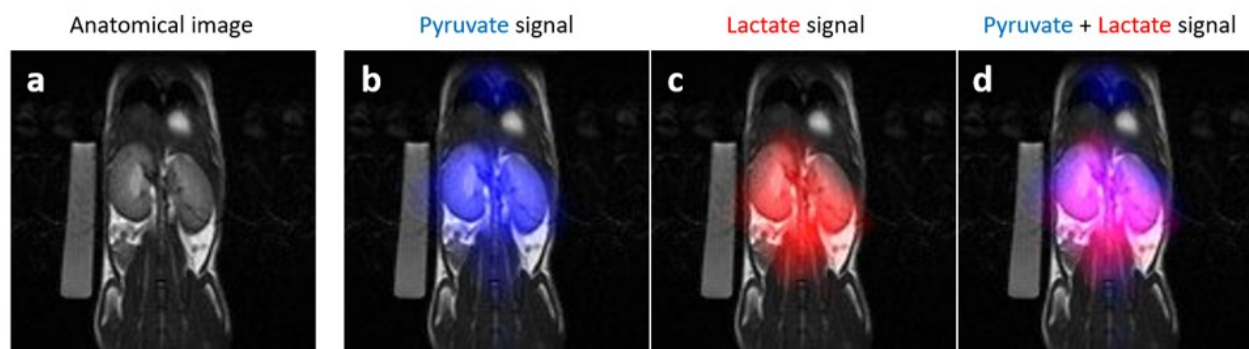


Figure 1. ¹³C- CSI using hyperpolarized [1-¹³C]pyruvate. a) anatomical T₂-weighed TurboRARE image, a phantom containing ¹³C-urea (thermally polarized) can be seen on the left. The pyruvate (b), lactate (c) and both (d) maps are overlapped with the anatomical image.

Conclusions

The attainment of a fully biocompatible solution of hyperpolarized [1-¹³C]pyruvate, free from toxic solvents and metal complexes, makes parahydrogen hyperpolarized [1-¹³C]pyruvate a promising tool for metabolic studies. In order to increase the hyperpolarization level, the hydrogenation conditions and the catalyst have to be further investigated.

References

- [1] F. Reineri, T. Boi and S. Aime "ParaHydrogen Induced Polarization of ¹³C carboxylate resonance in acetate and pyruvate" Nat.Comm. 2015.
- [2] E. Cavallari, C. Carrera, S. Aime and F. Reineri "13C MR Hyperpolarization of Lactate by Using ParaHydrogen and Metabolic Transformation in Vitro" Chem. Eur.J. 2016.
- [3] O. Bondar, E. Cavallari, C.Carrera, S. Aime, F. Reineri "Effect of the hydrogenation solvent in the PHIP-SAH hyperpolarization of [1-13C]pyruvate" Cat.Today 2021.

Molecular brain imaging with engineered hemodynamics

Robert Ohlendorf, Miriam Schwalm and Alan Jasanoff

Department of Biological Engineering, Massachusetts Institute of Technology, Cambridge MA

Introduction | How the mammalian brain processes information, stores memories and maintains homeostasis depends on the dynamic communication between neurons, glia cells, blood vessels and many other cell types via signaling molecules such as neurotransmitters, neuropeptides and hormones throughout the entire brain. Currently no technology can measure brain-wide molecular signaling with sufficient spatial and temporal resolution in living mammals, which poses a major roadblock for understanding molecular foundations of brain function and dysfunction in disease states.

Methods | Hemodynamic imaging using functional magnetic resonance imaging (fMRI) or functional ultrasound (fUS) represents the gold standard for imaging whole-brain function in animals and humans and the only method that can measure brain-wide function with a temporal resolution of single seconds and in-plane spatial resolution of $100 \mu\text{m}^{1,2}$. Yet, hemodynamic imaging lacks critical information on molecular pathways or signaling molecules underlying the measured imaging signals. We leverage the power of hemodynamic imaging and provide it with molecular information by engineering protein-based sensors (AVATar)³ that convert target molecular signal into hemodynamic imaging contrast in fMRI, ultrasound, or optical imaging (Figure 1A). We apply AVATars for molecular brain imaging in living rats using T_2^* -weighted MRI.

Results/Discussion | AVATars induce hemodynamic signals in response to target molecules at low nanomolar doses approaching sensitivity of nuclear imaging probes, without using radioactive or metallic components. The sensitive *in vivo* detection of AVATars allows brain delivery via non-disruptive infusion routes. Here, we develop an alternative fully genetically-encodable AVATar design which can be directly expressed *in situ* (Figure 1A). The design uses a protein architecture which reversibly cages the vasoactive pituitary adenylate cyclase activating peptide (PACAP) through an analyte-dependent, allosteric mechanism. Elevated analyte levels activate the AVATar and allow PACAP to bind receptors on vascular smooth muscle cells, causing local and transient vasodilation, and a hemodynamic imaging signal.

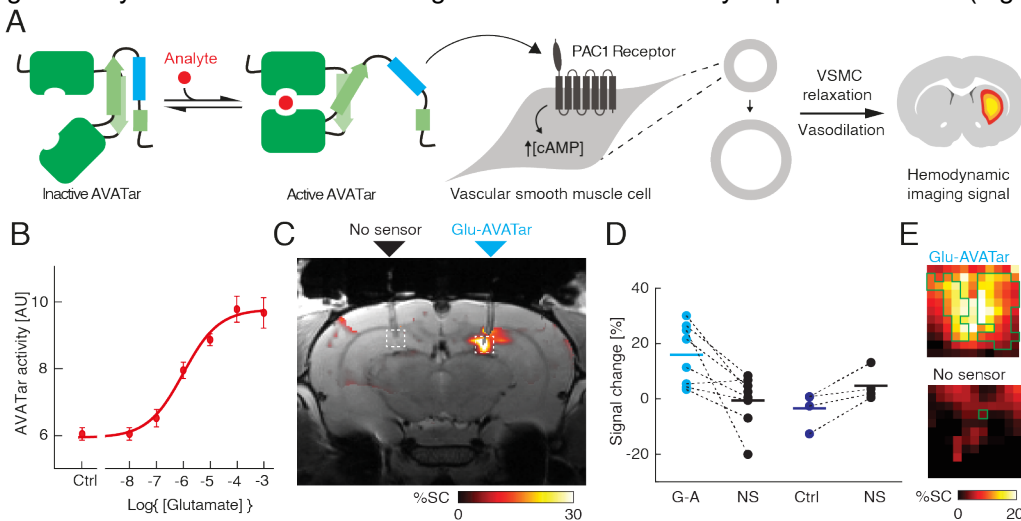


Figure 1: Neurotransmitter imaging with genetically-encodable AVATar. **A** Functional mechanism of a genetically-encodable AVATar. AVATars use vasoactive PACAP peptides (cyan) that trigger hemodynamic imaging contrast by acting at nanomolar concentrations on vascular smooth muscle cell receptors. Genetic fusion to a protein domain (green) reversibly cages PACAP in an analyte-dependent fashion. **B** Glutamate response of glutamate-responsive AVATar (Glu-AVATar) *in vitro*. **C** MRI response of AVATar in a rat to glutamate (red arrow) or buffer control (black arrow). **D** Group data of glutamate response of Glu-AVATar in MRI compared to no sensor (NS) or inactive control AVATar (Ctrl). **E** Average MRI signal changes in ROIs from group data in **D**.

Conclusion | AVATars facilitate multi-modal and multi-scale imaging of molecular brain function in living mammals. AVATars provide a bridging technology between brain-wide functional imaging with fMRI and highly sensitive, molecular nuclear imaging. The approach complements spatiotemporally highly precise, but locally-confined fluorescence imaging to visualize brain-wide molecular signaling dynamics that shape healthy and pathological brain function.

References

1. Ogawa, S., Lee, T. M., Kay, A. R. & Tank, D. W. Brain magnetic resonance imaging with contrast dependent on blood oxygenation. *Proc. Natl. Acad. Sci. U. S. A.* **87**, 9868–9872 (1990).
2. Macé, E. *et al.* Functional ultrasound imaging of the brain. *Nat. Methods* **8**, 662–664 (2011).
3. Ohlendorf, R. *et al.* Target-responsive vasoactive probes for ultrasensitive molecular imaging. *Nat. Commun.* **11**, 2399 (2020).

Molecular MRI for early detection of disease activity in liver fibrosis and response to treatment

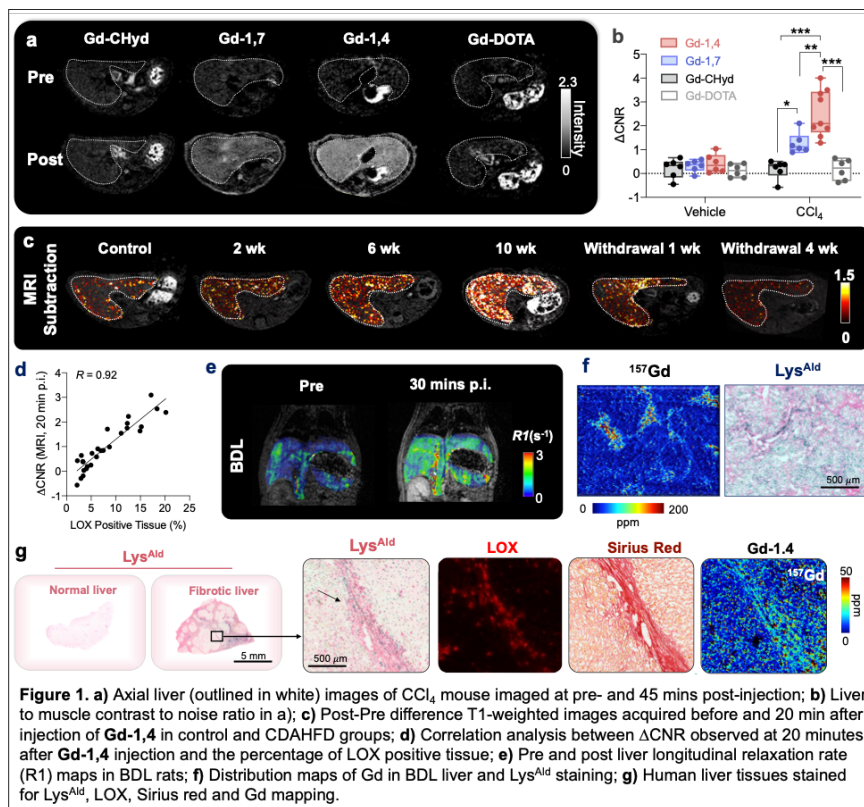
Yingying Ning,¹ Iris. Y. Zhou,¹ Jesse D. Roberts,² Nicholas J. Rotile,¹ Eman Akam,¹ Stephen C. Barrett,³ Mozhdeh Sojoodi,³ Matthew N. Barr,⁴ Tracy Punshon,⁴ Pamela Pantazopoulos,¹ Hannah K. Drescher,⁵ Brian P. Jackson,⁴ Kenneth K. Tanabe,³ Peter Caravan^{1,*}

¹ Athinoula A. Martinos Center for Biomedical Imaging, Institute for Innovation in Imaging, Department of Radiology, Massachusetts General Hospital and Harvard Medical School, Boston, MA 02129, USA, ² Cardiovascular Research Center of the General Medical Services, Massachusetts General Hospital and Harvard Medical School, Boston, MA 02129, USA, ³ Division of Surgical Oncology, Massachusetts General Hospital Cancer Center and Harvard Medical School, Boston, MA 02114, USA, ⁴ Department of Earth Sciences, Dartmouth College, Hanover, NH 03766, USA, ⁵ Gastrointestinal Unit, Massachusetts General Hospital and Harvard Medical School, Boston, MA 02114, USA

Introduction: Liver fibrosis is a progressive form of most chronic liver diseases that forms because of an aberrant wound healing response and results in a buildup of extracellular matrix (ECM).¹ Currently there are no noninvasive methods to assess fibrosis activity, i.e. fibrogenesis, or to sensitively detect early onset of fibrosis.² In ECM remodeling, lysine pairs in collagen will be oxidized by lysyl oxidase (LOX) to allysine aldehyde (Lys^{Ald}) and undergo cross-linking.³ We hypothesized that dual Lys^{Ald} would be a biomarker of fibrogenesis and thus designed a dual binding MRI molecular probe for non-invasive detection of Lys^{Ald} *in vivo*. The probe was tested in toxin- and dietary-induced mouse model, biliary stasis induced rat model of liver fibrogenesis and human fibrotic liver tissues.

Methods: **Synthesis:** Gd-1,4 and Gd-1,7 are Gd-DOTA derivatives with two hydrazine arms but different orientation. Gd-CHyd contains only one hydrazine arm.⁴ **Animal models:** Toxin-induced liver fibrosis: Male C57BL/6 mice were gavaged with CCl₄ or olive oil for 12 weeks. Dietary-induced live fibrosis: Male C57BL/6 mice were fed choline-deficient, L-amino acid-defined, high-fat diet (CDAHFD) for 2, 6, 10 weeks (N = 6 per group), or standard chow (N = 10). Two additional received CDAHFD for 10 weeks and then standard chow for 1 or 4 weeks. Biliary stasis rat model: Liver fibrosis was induced in male CD rats (N = 7) by bile duct ligation (BDL), and control animals (N = 4) underwent a sham procedure. Human liver tissue: Fibrotic/cirrhrotic liver associated with NASH (N = 5) and normal liver tissue (N = 4) were obtained from surgery. **In vivo MRI:** Animals were imaged with a 4.7 Tesla Bruker MRI scanner. 3D T1-weighted FLASH images were acquired prior to and up to 30-50 minutes post i.v. 100 μmol/kg Gd-1,4.

Results: Among the different probes designed here, Gd-1,4 shows the highest on rate, relaxivity and lower off rate with Lys^{Ald} bearing protein BSA^{Ald} *in vitro*. *In vivo* probe screening in CCl₄ induced liver fibrosis mice confirmed the highest sensitivity and specificity of Gd-1,4 in detecting fibrogenesis (Fig 1a,b). In CDAHFD mouse model, Gd-1,4 MRI can detect early onset of disease as early as 2 weeks on CDAHFD and measure early response to treatment (withdraw the diet for one week, Fig 1c). We found that Gd-1,4 enhanced MRI tracked well with fibrogenesis markers including LOX (R = 0.92, P < 0.0001, Fig. 1d), Lys^{Ald} and α-SMA. Then we tested the probe in a rat model of biliary stasis and the change of liver longitudinal relaxation rate ΔR1 were significantly enhanced in the BDL animals compared to sham rats (Fig. 1e). *Ex vivo* analyses on rat liver tissues using LA-ICP-MS showed that the probe specifically accumulates in the fibrotic septa which colocalized with the presence of Lys^{Ald} (Fig. 1f). We incubated human liver tissues with Gd-1,4 and observed similar results. The average Gd concentration in Lys^{Ald} positive areas was significantly higher than in regions of low Lys^{Ald}, giving the overall Gd concentration much higher in fibrotic liver (Fig. 1g).



Discussion and conclusion: The rationally designed MR probe Gd-1,4 has two hydrazine moieties that can form reversible covalent hydrazone bonds with two Lys^{Ald} residues. The dual binding capability results in faster on-rate, slower off-rate, and higher protein-bound relaxivity. Altogether this leads to markedly superior performance for detection of liver fibrogenesis *in vivo*. The Gd-1,4 enhanced MRI signal was reflective of LOX mediated Lys^{Ald} cross-linking related disease activity. In a dietary mouse model of NASH, Gd-1,4 molecular MRI could detect the early onset of liver fibrosis prior to significant buildup of collagen and was very sensitive to a reduction in fibrogenesis following a therapeutic intervention. The MR signal change observed with Gd-1,4 is robust across different models and species. *Ex vivo* analysis of human liver specimens shows absence of extracellular aldehyde in healthy liver, but high concentrations in fibrotic liver. LA-ICP-MS experiments on human fibrotic liver reveal Gd concentrations similar to that observed in rat model, strongly suggesting that robust MR signal changes would be seen in patients with chronic liver disease, indicating the high clinical translation potential of Gd-1,4.

References: 1) Pellicoro, A., Ramachandran, P., Iredale, J.P. & Fallowfield, J.A. *Nat Rev Immunol* 2014, 14, 181-194; 2) Tapper, E.B. & Lok, A.S. *N Engl J Med* 2017, 377, 756-768; 3) Bonnans, C., Chou, J. & Werb, Z. *Nat Rev Mol Cell Biol* 2014, 15, 786-801; 4) Akam, E. A., Abston, E., Rotile, N. J., Slattery, H. R., Zhou, I. Y., Lanuti, M., & Caravan, P. *Chem. Sci.* 2020, 11, 224-231.

Redox-responsive transition metal MRI probes: from liposomes to small molecules

Janet R. Morrow,¹ Md Saiful I. Chowdhury¹, Jaclyn Raymond¹, Joseph Spornyak²

¹Chemistry Department, The State University of New York at Buffalo, New York, USA

²Department of Cell Stress Biology, Roswell Park Comprehensive Cancer Center, Buffalo, New York 14263, USA

Introduction: Redox-responsive MRI contrast agents would be a valuable addition to the arsenal of molecular MR probes. Several years ago, we introduced a Co(II)/Co(III) paraCEST agent that switched from paramagnetic Co(II) to diamagnetic Co(III) in the presence of O₂.¹ Macrocyclic Fe(II)/Fe(III) complexes also have electrode potentials that can be tuned by 2 V towards the production of responsive probes. In these couples, the Fe(II) complex is a paraCEST or shift agent and Fe(III) complexes are paraCEST, shift or T₁/T₂ agents.^{2,3} Recently we have shown that transition metal shift agents such as Co(II) or Fe(II) can be loaded into liposomes to produce lipoCEST agents⁴ whereas Fe(III) liposomes are T₁/T₂ MRI probes in mice.³ Here we show that liposomal iron complexes accumulate in tumors towards redox-responsive agents for tumor characterization.

Methods: Liposomes were made of 40 mM lipids (DPPC : DSPE-PEG : Amphiphilic complex : Cholesterol = 64:6:15:15.) and 40 mM iron complex for hydration. Liposomes were extruded to 100 nm, sonicated, subjected to ultra-filtration at 100 kDa cut-off. The Z spectra were collected on a 400 MHz NMR spectrometer. Asymmetry from these Z spectra was calculated to extract the saturation transfer peak. In vivo imaging studies were on a 4.7 T Bruker preclinical MRI in healthy mice (BALB/cJ, Jackson Laboratory) and mice with CT26 tumors. Two scan procedures were used: (1) a T₁-weighted, three-dimensional (3D), spoiled gradient echo scan covering the mouse from the thorax to tail to determine signal enhancement and (2) T₁ relaxometry using an IR-SSFP.

Results: Transition metal shift agents loaded into liposomes produce large intraliposomal water proton shifts. Typically, hydroxalkyl pendants in macrocyclic complexes produce superior shifts. Treatment of the paramagnetic liposomes with peroxide to oxidize the Co(II) or Fe(II) complex changes the position of the saturation transfer asymmetry as a function of the electrode potential of the interior complex versus the amphiphilic complex. To track the liposomes in vivo, Fe(III) complexes were added into the bilayer and interior of the liposome. Accumulation of the MRI probes in murine CT26 tumors is shown by using T₁ weighted imaging (Figure 1). Studies of liposomal iron complexes that are peroxide responsive agents

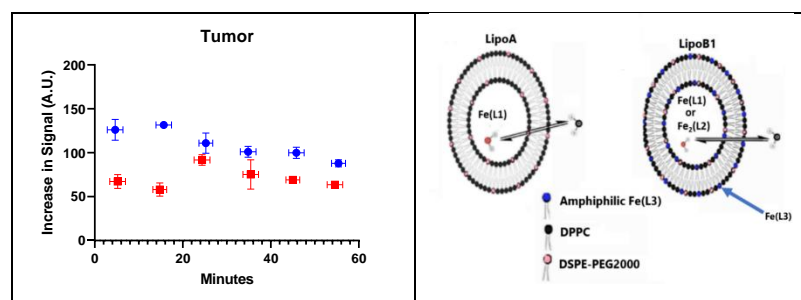


Figure 1. Increase in signal over time in murine CT26 tumors for two different liposomal iron complexes. Scheme of liposomes.

through switching oxidation state will be presented as MRI probes for murine tumor models.

Conclusions: Transition metal complexes with tunable electrode potentials are a promising type of molecular imaging probe.

Liposomes have an essential role in the formation of the responsive probes and their accumulation in tumors for imaging studies.

References. 1. Tsitovich, P. B.; Spornyak, J. A.; Morrow, J. R. *Angew. Chem. Int. Ed.* **2013**, *52*, 13997 – 14000 2. Tsitovich, P. B.; Gendron F.; Nazarenko, A. Y.; Livesay, B. N.; Lopez, A. P.; Shores, M. P.; Autschbach, J. A.; Morrow, J. R., *Inorg. Chem.* **2018**, *57*, 8364-8374. 3. Abozeid, S. M.; Asik, D.; Sokolow, G. E.; Nazarenko, A. Y.; Lovell, J. F.; Morrow, J. R., *Angew. Chem. Int. Ed.* **2020**, *59*, 12093-97. 4. Abozeid, S. M.; Chowdhury, M. S. I.; Asik, D.; Spornyak, J. A.; Morrow, J. R. *ACS Appl. Bio Mater.* **2021**, *4*, 11, 7951–7960.

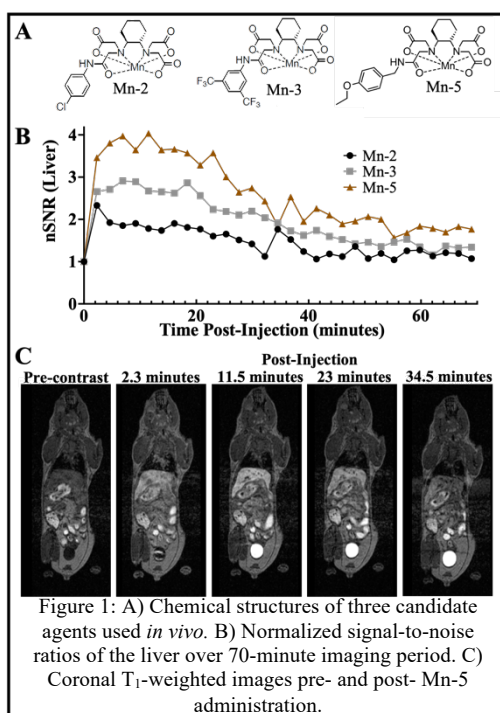
The development of novel OATP1-targeted manganese-based MRI contrast agents

Sean W. McRae¹, Francisco M. Martinez², Michael B. Cleary³, Peter Caravan³, Eric M. Gale³, John A. Ronald^{1,2}, Timothy J. Scholl^{1,2,4}

¹Department of Medical Biophysics, Western University, London, Ontario, Canada. ²Robarts Research Institute, Western University, London, Ontario, Canada. ³Martinos Center for Biomedical Imaging, Massachusetts General Hospital, Boston, Maine, United States. ⁴Ontario Institute for Cancer Research, Toronto, Ontario, Canada.

Introduction: *In vivo* molecular imaging requires highly sensitive imaging technologies paired with optimized molecularly targeted imaging probes. Clinical magnetic resonance imaging (MRI) is the standard for detection of macroscopic pathologies but due to its limited inherent sensitivity it often requires imaging probe doses that can be challenging for the development of new probes. For instance, recent concerns over gadolinium deposition in patients with renal impairments, has shifted the focus to the development of new agents containing other paramagnetic ions such as manganese. Gadolinium-ethoxybenzyl-diethylenetriamine pentaacetate (Gd-EOB-DTPA; *Primovist*) is a liver-targeted agent that is transported into hepatocytes primarily by organic anion transporting polypeptide 1B1 and 1B3 (OATP1B1 and OATP1B3). Our group has shown that engineering cells to express human OATP1B1 or 1B3 increases their detectability on T₁-weighted images upon administration of Gd-EOB-DTPA. Here we developed and evaluated a suite of amphiphilic manganese agents both *in vitro* for relaxivities and human OATP targeting, as well as *in vivo* for liver imaging in mice.

Methods: **Agent synthesis:** Five agents (that will be referred to as Mn 1 – 5) were derived from a *trans*-cyclohexylene-1,2-diamine-*N,N,N',N'*-tetraacetate-type chelator that binds Mn²⁺ ions with high affinity and possesses high relaxivity. Lipophilic side chains were varied to increase the overall amphiphilicity of the molecule to promote uptake through OATP. **Cellular engineering:** Human breast cancer (MDA-MB-231) cells were engineered using a lentiviral vector expressing fluorescent zsGreen to facilitate cell sorting, and either the human OATP1B1 or OATP1B3. **In vitro agent characterization:** Agent relaxivity was measured at low field (0.23 mT – 1 T) using fast-field cycling relaxometry, and at our imaging field strength (3 T) using a fast-spin echo inversion-recovery sequence (FSE-IR) at 37°C (data not shown). Naïve and engineered (containing one of the two OATP isoforms noted above) MDA-MB-231 cells were incubated with one of the novel manganese-agents (1.6 mM) for 90 minutes, then washed and collected for analysis. An FSE-IR sequence was used to acquire R₁ maps of cell pellets to assess agent uptake through OATP. Based on the *in vitro* uptake data, Mn-2, Mn-3, and Mn-5 were identified as the best candidates for use *in vivo* (Figure 1A). **In vivo MRI:** Healthy BALB/c mice (Charles River Laboratories) were imaged using a custom-built whole-body linear birdcage coil. We sought to evaluate endogenous uptake of agent through murine OATP transport as well as biodistribution and blood clearance in mice. Animals were anaesthetized using isoflurane, catheterized through the tail vein, and placed on a temperature-controlled bed for imaging. Pre-contrast images were taken before agent administration using a 3D spoiled gradient recalled steady state acquisition (3D-SPGR) ($\alpha = 60^\circ$, TE/TR 2.5/14.7 ms, NEX 1). A 0.1 mmol/kg dose of agent was administered before dynamic T₁-weighted imaging of agent biodistribution for 70 minutes.



Results: The mean relaxivity of the five manganese agents at 3 T was $2.99 \pm 0.3 \text{ mM}^{-1}\text{s}^{-1}$. *In vitro* uptake assays through human transporters showed uptake of all five manganese-based agents compared to cells lacking the transporter. Preferential uptake through the OATP1B1 isoform of the transporter was observed in all *in vitro* trials. Agent uptake was estimated by dividing the change in relaxation rates between the naïve and treated cells by the relaxivity of the agent at 3 T and normalized to the uptake of *Primovist* through OATP1B3 (our benchmark). This uptake parameter showed higher uptake of Mn agents through OATP1B1 compared to our *Primovist*-OATP1B3 benchmark. *In vivo* MRI showed mixed renal/hepatobiliary clearance with peak nSNR values in the liver at 2.3, 6.9 and 11.3 minutes for Mn-2, Mn-3, Mn-5, respectively (Figure 1B). Mn-5, the agent containing the ethoxy benzyl side chain displayed the highest peak nSNR value in the liver (4-fold increase relative to pre-contrast liver at 11.3 minutes).

Discussion: The affinities of five novel agents to the OATP family of transporters were assessed here *in vitro* using human-derived OATPs, and *in vivo* liver uptake of agents presumably through endogenous mouse-OATPs. The *in vitro* data show that despite the lower relaxivity of the five Mn-agents at 3 T compared to *Primovist*, the agents provided strong R₁ enhancement, suggesting high uptake and retention through OATP. The *in vitro* uptake data also suggested that the manganese-derived agents had preferential uptake through the OATP1B1 transporter over 1B3, the opposite behaviour of *Primovist*. The rapid uptake and clearance of these agents seen *in vivo* helps support the hypothesis that these newly synthesized agents had high affinity for the OATP transporters (Figure 1C).

Conclusions: These next-generation Mn-derived contrast agents display promising characteristics and offer a potential solution to reduce Gd-specific concerns that are associated with commercially available agents.

The novel agents investigated showed good uptake through human OATP1B1 *in vitro* and successfully generated strong liver contrast *in vivo*, showing fast clearance, and no evident toxicity at 0.1 mmol/kg. In a future study, we hope to evaluate the uptake of these agents in tumour models engineered to express OATP1B1, at higher administered manganese doses.

References: 1) Patrick P, et al. Dual-modality gene reporter for *in vivo* imaging. *Proceedings of the National Academy of Sciences*, **2014**. 2) Nyström N et al. Longitudinal Visualization of Viable Cancer Cell Intratumoral Distribution in Mouse Models Using Oatp1a1-Enhanced Magnetic Resonance Imaging. *Invest Radiol*, **2019**. 3) Grobner T. Gadolinium-a specific trigger for the development of nephrogenic fibrosing dermopathy and nephrogenic systemic fibrosis? *Nephrol Dial Transplant*, **2006**.

Using dynamic contrast-enhanced MR-CEST urography for detecting changes in kidney function following urinary tract obstruction

Julia Stabinska^{1,2}, Aruna Singh^{1,2}, Zinia Mohanta^{1,2}, Nora Haney³, Farzad Sedaghat², Max Kates³, Yuguo Li^{1,2}, Michael T. McMahon^{1,2}

¹F.M. Kirby Research Center for Functional Brain Imaging, Kennedy Krieger Institute, Baltimore, MD, USA, ²Division of MR Research, Department of Radiology, The Johns Hopkins University School of Medicine, Baltimore, MD, USA, ³The James Buchanan Brady Urological Institute, Department of Urology, The Johns Hopkins University School of Medicine, Baltimore, MD, USA

Introduction: Urinary tract obstructions (UTOs) are blockages in the urinary tract that impede normal urine flow, causing urinary retention and increased retrograde pressure¹. Because the extent of recovery of renal function depends on severity and duration of obstruction, early diagnosis and intervention are crucial for preventing irreversible kidney damage¹. While effective in characterizing the upper tract, ultrasonography and traditional CT are limited in quantifying kidney function². Renal scintigraphy can be applied for assessment of differential kidney function but its anatomical resolution is poor². In contrast, iopamidol-enhanced chemical exchange saturation transfer (CEST) MRI has been shown to provide functional information by generating spatially localized renal pH maps and time-activity curves^{3,4,5}. In this study, we explore the potential of dynamic contrast-enhanced MR-CEST urography in mice with UO.

METHODS: For the in vivo study, the right ureter of six mice was obstructed via suture ligation and animals imaged at day 1 (3 mice) and 2 (3 mice) post-obstruction on a 11.7 T Bruker MRI scanner. A total of 204 CEST images, including twelve M₀ images and 96 sets of saturated images at 4.3 and 5.5 ppm were collected with: B₁ = 3.6 μT, t_{sat} = 3sec, TE/TR = 3.49/5125 msec, matrix: 64x64, slice thickness: 1.5 mm, RARE factor: 32. Iopamidol was injected via tail-vein catheter. Renal time-course enhancement curves were measured as a percentage change in the post-injection

CEST- signal at 4.3 ppm relative to the average pre-injection signal. For pH mapping, saturation transfer ratio (ST_{Ratio}) at 4.3 and 5.5 ppm was quantified from three averaged images collected at the peak enhancement time. Averaged pre-injection maps were then subtracted from the post-injection images to remove endogenous signals. Renal pH values were obtained using a calibration curve as described previously³.

Results: For the healthy mice, the dynamic CEST curves of both kidneys were nearly identical and displayed rapid excretion. The representative renal pH map and histogram displayed similar acidity for both kidneys (pH 6.71 ± 0.06 and 6.68 ± 0.08, **Fig. 1**). In UO mice, the time-activity curve for the obstructed kidneys displayed prolonged contrast excretion and decreased ST_{ratio} values. These time-activity curves showed clear differences between the healthy and UO kidneys

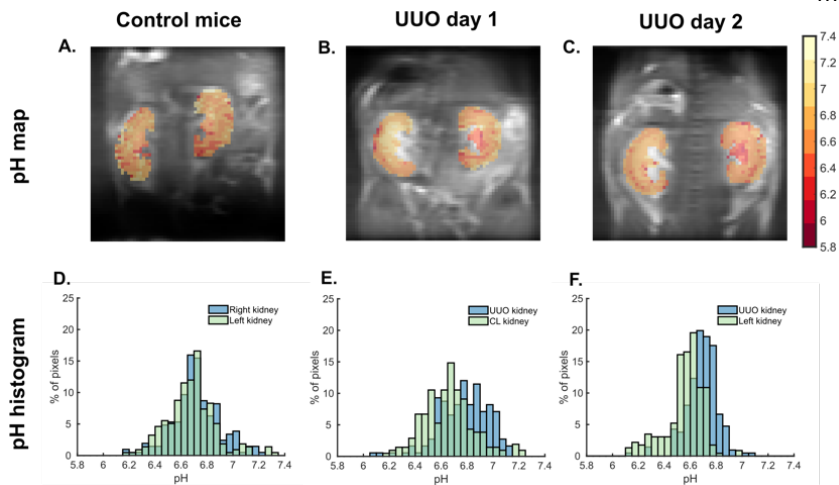


Figure 1: pH maps and pH histograms measured in (A, D) a control mouse, (B, E) UO mice at day 1 and (C, F) day 2 after obstruction.

which reflects the uptake and excretion of iopamidol differences. At one day after UO, there was an increase in pH values in the obstructed kidney, especially in the inner and outer medulla, compared with the contralateral (pH 6.77 ± 0.05 and 6.66 ± 0.05 in the UO and CL kidney, respectively). The same trend could be observed at day 2 after obstruction (pH 6.69 ± 0.05 and 6.56 ± 0.04 in the UO and CL kidney, respectively). Box-plot analysis for all six UO mice revealed increased pH values in the UO kidneys compared with the native kidney.

Discussion: We have applied DCE-MR CEST urography to a murine model of obstructive nephropathy and non-invasively assessed kidney function over 2 days after UO. Our results demonstrate that a dynamic CEST acquisition combined with a single injection of iopamidol allows simultaneous measurements of both renal perfusion and pH, as opposed to the conventional diagnostics, which provide only one type of metric to characterize kidney function. As early as one day after UO, we observed both increased pH values, which are likely due to tubular defects in urinary acidification and retention of iopamidol in the renal parenchyma of the UO kidney, which suggests a decline in renal function. Overall, these results suggest that CEST imaging might be particularly useful for monitoring progression of renal injury caused by UTOs. We believe that our dynamic CEST MRI protocol is promising for early assessment of upper UTOs and could be translated to patients with obstructive nephropathy.

CONCLUSION: Our findings indicate that DCE-MR-CEST urography can detect changes in renal filtration and pH homeostasis and distinguish between obstructed and unobstructed kidney as early as one day after UO.

REFERENCES: 1) Brenner BM et al., . the Kidney. 8th ed. Saunders Elsevier; 2008; 2) Bo S et al. Dynamic Contrast Enhanced-MR CEST Urography: An Emerging Tool in the Diagnosis and Management of Upper Urinary Tract Obstruction. Tomography. 2021;7(1):80-94 ; 3) Pavuluri K et al. Noninvasive monitoring of chronic kidney disease using pH and perfusion imaging. Sci Adv. 2019;5(8):eaaw8357; 4) Irrera P et al. Dual assessment of kidney perfusion and pH by exploiting a dynamic CEST-MRI approach in an acute kidney ischemia-reperfusion injury murine model. NMR Biomed. 2020 Jun;33(6):e4287; 5) Tantawy MN et al. Assessment of renal function in mice with unilateral ureteral obstruction using ^{99m}Tc-MAG3 dynamic scintigraphy. BMC Nephrol 13, 168 (2012);

Manganese-based blood pool T1 contrast-agent from a single pot template reaction

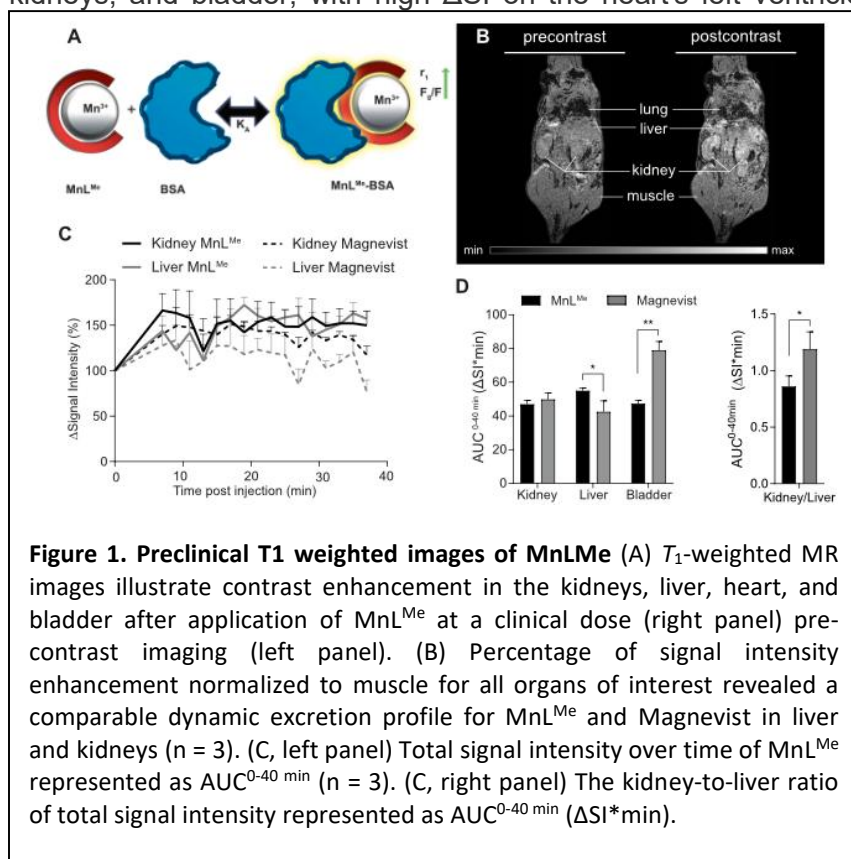
Anbu Sellamuthu¹, Sabrina Hoffmann², Fabio Carniato³, Thomas Price⁴, Lawrence Kenning⁵, Timothy Prior¹, Mauro Botta³, Graeme Stasiuk⁴, Andre F. Martins^{2,6}

¹University Of Hull, HULL, United Kingdom; ²University of Tübingen, Tübingen, Germany; ³Università del Piemonte Orientale 'A. Avogadro', Dipartimento di Scienze e Innovazione Tecnologica, Alessandria, Italy; ⁴King's College London, Imaging Chemistry and Biology, London, United Kingdom; ⁵Hull Royal Infirmary Hospital NHS Trust, Hull, United Kingdom; ⁶Cluster of Excellence iFIT (EXC 2180) "Image-Guided and Functionally Instructed Tumor Therapies", University of Tübingen, Germany.

Introduction: Gadolinium-based T_1 contrast agents (GdCAs) are the gold standard for clinical contrast-enhanced MRI applications.¹ However, due to poor stability in acyclic GdCAs, leading to free-Gd³⁺ toxic effects,² research has focused on Gd³⁺-free CAs. Manganese-based MnCAs are perceived as ideal alternative CAs³ to GdCAs as Mn²⁺ is biogenic with near equivalent MRI contrast efficacy. Therefore, we have developed a novel and stable MnCA (**MnLMe**) through a single pot template reaction and studied its properties as an MRI contrast agent both *in vitro* and *in vivo*.⁴

Methods: We designed and synthesized a novel pentadentate type Mn²⁺ complex **MnLMe** utilizing a single-pot template strategy unique to the field of contrast agent design. **MnLMe** has been studied in both its structural and physicochemical properties. The relaxometry properties (longitudinal relaxation times (T_1), water proton relaxation rates ($r_1 = 1/T_1$) and proton relaxivity enhancement (PRE)) and kinetic inertness of the **MnLMe** were ascertained by both ¹H-NMR (JEOL-400 MHz) and ¹H-NMRD (Stelar) methods. Phantom and murine MR images were acquired on a 7 T preclinical MR scanner (Bruker BioSpec 70/30, Bruker BioSpin, Ettlingen, Germany) using an 86-mm diameter 1H transceiver volume coil (Bruker). T_1 -weighted pre- and post-contrast *in vivo* MR images were acquired with a 3D FLASH-sequence strategy.

Results/Discussion: **MnLMe** synthesised in a one-pot reaction, shows relaxivity (r_1) of 4.2 and 4.9 mM⁻¹ s⁻¹ at 400 MHz (9.4 T) and 64 MHz (1.5 T), respectively, with a $q = 2$. **MnLMe** shows inertness to transmetallation and transchelation at neutral pH. Interestingly, **MnLMe** displays higher inertness ($k = 8.9 \times 10^{-3}$ s⁻¹) than [Gd(DTPA)(H₂O)]²⁻ ($k = 1.6 \times 10^{-2}$ s⁻¹) (25 equiv Zn²⁺). The ¹H-NMRD profile of **MnLMe** is typical of monomeric, low molecular weight complexes. It also displays enhanced $r_1 = 21.1$ mM⁻¹ s⁻¹ (20 MHz, 298 K, pH 7.4) upon binding to BSA ($K_a = 4.2 \times 10^3$ M⁻¹), with a reduced water exchange rate switching from a $q = 2$ to a $q = 1$ species, confirming the albumin binding. Preclinical MRI studies show elimination through the liver, kidneys, and bladder, with high ΔSI on the heart's left ventricle suggesting binding to albumin *in vivo*. The



enhanced r_1 and *in vivo* MRI suggest that **MnLMe** is capable of being a blood pool agent and comparable to the clinically available Gd based contrast agents.

Conclusions: This is the first example to date of a template reaction used for MRI contrast agent synthesis. This study confirms that the **MnLMe** is kinetically inert under neutral pH conditions, when stressed with other chelators and endogenous metal ions. **MnLMe** has been shown to interact with albumin proteins and *in vivo* shows delayed clearance from the blood with observed high ΔSI on the heart's left ventricle, thus **MnLMe** could be used as blood pool agent.

References: [1] Matsumura et al., *Magn. Reson. Med. Sci.* **2013**, 12(4), 297. [2] (a) Clough et al., *Nature Commun.* **2019**, 10, 1420. (b) Thakral et al., *Contrast Media Mol. Imaging* **2007**, 2, 199. (c) Thomsen et al., *Clin. Radiol.* **2006**, 61(11), 905. (d) Grobner, T. *Nephrol. Dial. Transplant* **2006**, 21(4), 1104. [3] Gale et al., *Radiology* **2018**, 286, 865. [4] Anbu et al., *Angew. Chem. Int. Ed.* **2021**, 60, 10736–10744.